Precambrian Research 313 (2018) 205–220

Contents lists available at ScienceDirect

Precambrian Research

journal homepage: www.elsevier.com/locate/precamres

Testing models of pre-GOE environmental oxidation: A Paleoproterozoic marine signal in platform dolomites of the Tongwane Formation (South Africa)

Matthew R. Warke[a,b,*], Stefan Schröder[a], Harald Strauss[c]

[a] Basin Studies and Petroleum Geoscience, School of Earth and Environmental Sciences, University of Manchester, Manchester M13 9PL, United Kingdom
[b] School of Earth and Environmental Sciences, University of St Andrews, St Andrews KY16 9AL, United Kingdom
[c] Geologisch-Paläontologisches Institut der Westfälischen Wilhelms-Universität Münster, Corrensstraße 24, 48149 Münster, Germany

ARTICLE INFO

Keywords:
Tongwane Formation
Transvaal Supergroup
Great Oxidation Event
cerium anomalies
carbon isotopes

ABSTRACT

Carbonate facies of the upper Tongwane Formation preserve a largely overlooked record of pre-GOE Paleoproterozoic seawater. This inventory has survived despite a complex paragenetic history involving both diagenetic and contact metamorphic processes. BIF mineral assemblages are dominated by a medium-grade grunerite overprint and the formation of prograde and retrograde riebeckite. The massive dolomite member, a platform top carbonate which caps the succession, is characterized by marine REY_{SN} patterns lacking significant negative Ce_{SN} anomalies (< 10%) and $\delta^{13}C_{carb}$ values of between +1.83 and +2.95 $‰_{VPDB}$ that are slightly elevated above Paleoproterozoic 'normal marine' values. Systematically decreasing $\delta^{13}C_{carb}$ values measured in monotonously recrystallized, talc bearing, slope carbonates reflect interaction with devolatilization fluids during contact metamorphism caused by the intrusion of the Bushveld Igneous Complex; slope carbonates offer no insight into marine paleoredox conditions. Thus, despite contact metamorphism, Paleoproterozoic marine signals are retained in platform-top dolomites, however they do not support claims for widespread oxygen accumulation in shallow depositional environments of the Transvaal Basin on the eve of the GOE.

1. Introduction

The late Neoarchean to late Paleoproterozoic rise in oxygen, also known as the "Great Oxidation Event" (GOE; Holland, 2002; 2006), was arguably one of the most important paleoenvironmental changes in Earth history. Evidence for this rise in oxygen is recorded in numerous Neoarchean-Paleoproterozoic supracrustal successions that are preserved in modern-day North America, Western Australia, Fennoscandia, Brazil, and southern Africa (Martin et al., 2013; Gumsley et al., 2017). In southern Africa, the Neoarchean to Paleoproterozoic Transvaal Supergroup (Figs. 1 and 2) preserves a robust sedimentological archive that spans this paleoenvironmental transition (Eriksson et al., 2006).

Within the lower Transvaal Supergroup (Fig. 1) trace element concentrations and stable isotope trends within facies of the Campbellrand-Malmani carbonate platform suggest trace levels of oxygen were present (at least transiently) in Neoarchean depositional environments (Wille et al., 2007; Godfrey and Falkowski, 2009; Kendall et al., 2010; Voegelin et al., 2010; Eroglu et al., 2015). Higher in the succession – within the eastern Transvaal Basin – Paleoproterozoic strata of the Duitschland Formation and its debated lateral equivalent, the Rooihoogte Formation, record the disappearance of mass-independently fractionated sulfur (MIF-S) isotopes (Guo et al., 2009; Luo et al., 2016). Disappearance of the MIF-S signal, and its replacement with a dominant mass-dependent fractionation signal, indicates a rise in ozone, atmospheric oxygen, and marine sulfate concentrations (Farquhar et al., 2000, 2007). Additionally, in the upper Duitschland Formation, shallow-water dolomites record a prominent positive carbon stable isotope excursion of up to +10 $‰_{VPDB}$ (Buick et al., 1998; Bekker et al., 2001; Frauenstein et al., 2009; Guo et al., 2009), which may indicate oxygen accumulation due to rapid burial of organic carbon in another part of the basin (Des Marais et al., 1992). Understanding what happened in this interval, between the first 'whiffs' of photosynthetic oxygen production in the Neoarchean and the disappearance of the MIF-S signal in the Paleoproterozoic, is of vital importance for understanding the timing of the GOE (Bekker et al., 2004; Lyons et al., 2014).

Carbonates deposited in this interval may provide insight into seawater chemistry in the prelude to the GOE. Recent stratigraphic revision of the Transvaal Supergroup (Gumsley et al., 2017) suggests that three carbonate-bearing successions in the Transvaal Supergroup were

* Corresponding author at: School of Earth and Environmental Sciences, University of St Andrews, St Andrews KY16 9AL, United Kingdom.
E-mail address: mw438@st-andrews.ac.uk (M.R. Warke).

https://doi.org/10.1016/j.precamres.2018.04.015
Received 26 June 2017; Received in revised form 18 December 2017; Accepted 16 April 2018
Available online 18 April 2018

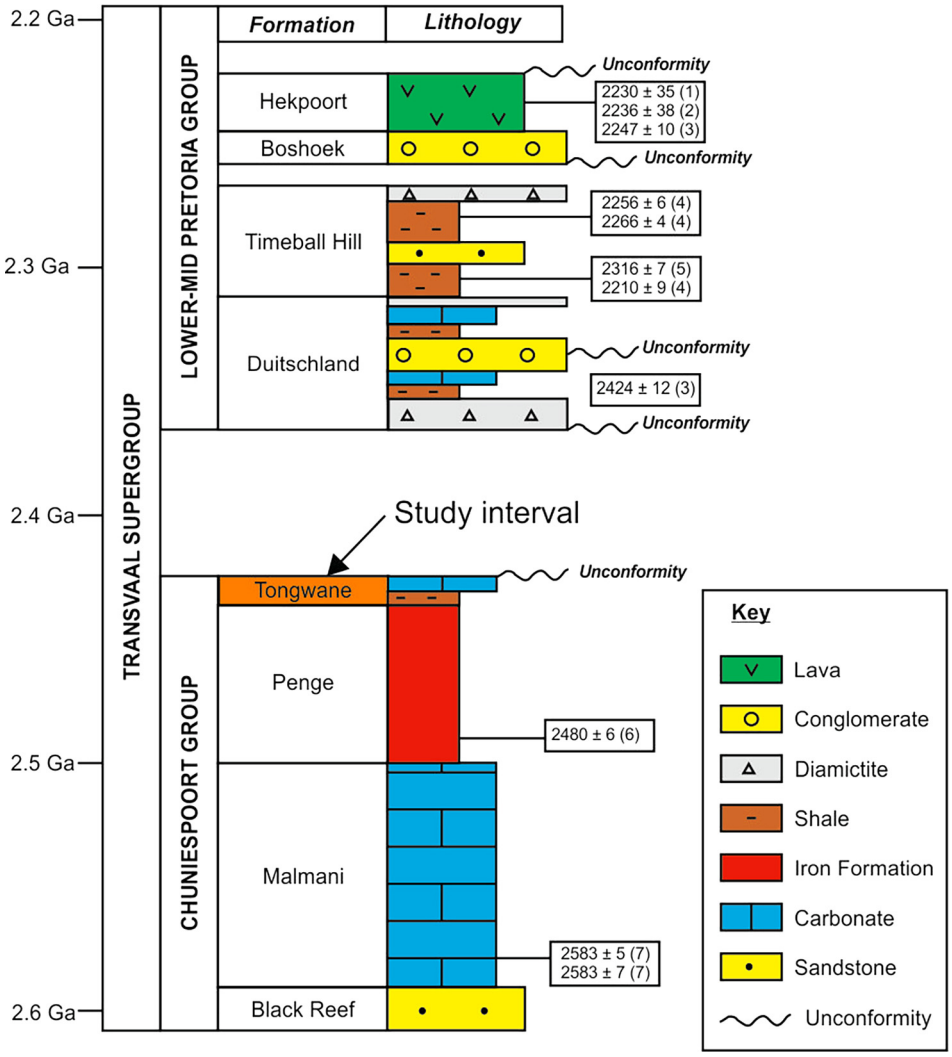

Fig. 1. Stratigraphic column of the Chuniespoort to mid Pretoria groups in the Transvaal Basin. Age data from: (1) Dorland (2004), (2) Cornell et al. (1996), (3) Schröder et al. (2016), (4) Rasmussen et al. (2013), (5) Hannah et al. (2004), (6) Nelson et al. (1999), (7) Martin et al. (1998).

deposited in the interval between the appearance of oxygen 'whiffs' in the Campellrand-Malmani platform and the disappearance of MIF-S signals in the Pretoria Group: (i) the Tongwane Formation (Schröder and Warke, 2016), (ii) the upper Koegas Subgroup (Schröder et al., 2011), and (iii) the Moodraai Formation (Bau et al., 1999; Tsikos et al., 2001).

While these carbonate-bearing successions are broadly coeval (Gumsley et al., 2017), their stratigraphic relations constrain relative age relationships. The Tongwane Formation is the oldest, on the basis that it conformably overlies the Penge Iron Formation and thus may be temporally equivalent to the lower Koegas Subgroup, the latter of which lacks carbonate units (Schröder et al., 2011). The Moodraai Formation significantly post-dates the upper Koegas carbonates, as the two successions are separated by a regional unconformity at the base of the Postmasburg Group and the Makganyene and Ongeluk formations (Moore et al., 2012). In addition to being temporally distinguishable, the three carbonate-bearing successions were also deposited in different depositional environments, with both the upper Koegas and Mooidraai successions being paleogeographically constrained to the Griqualand West Basin.

This contribution focuses on the oldest of these three successions, exclusively preserved in the eastern Transvaal Basin (Fig. 1): the platform carbonates of the Tongwane Formation. It has recently been proposed that small, positive $\delta^{13}C_{carb}$ anomalies of up to 3.5 $‰_{VPDB}$ (Bekker et al., 2001) measured in Tongwane Formation carbonates imply increased organic carbon burial and concomitant free oxygen production at the time of deposition (Gumsley et al., 2017). These authors propose a causal relationship between this inferred pulse of oxygen accumulation, oxidation and collapse of a methane-dominated greenhouse and the onset of pronounced icehouse conditions and glaciation (Gumsley et al., 2017). However, in the case of the Tongwane Formation only a small $\delta^{13}C_{carb}$ dataset is published (n = 6; Bekker et al., 2001; Guo et al., 2009) and, prior to this study, no detailed assessment of the succession's complex diagenetic and metamorphic history has been undertaken. Both diagenetic and metamorphic processes have the potential to alter the stable isotope record of Tongwane Formation carbonates.

The sedimentological framework, and bulk rock geochemistry, of the Tongwane Formation was recently discussed by Schröder and Warke (2016). This study expands upon that work by considering the paragenesis, trace element geochemistry and the carbon and oxygen stable isotope record preserved within carbonate facies. It demonstrates that the geochemistry of the Tongwane Formation provides valuable insight into the redox conditions of the eastern Transvaal Basin at the onset of the Paleoproterozoic rise in oxygen.

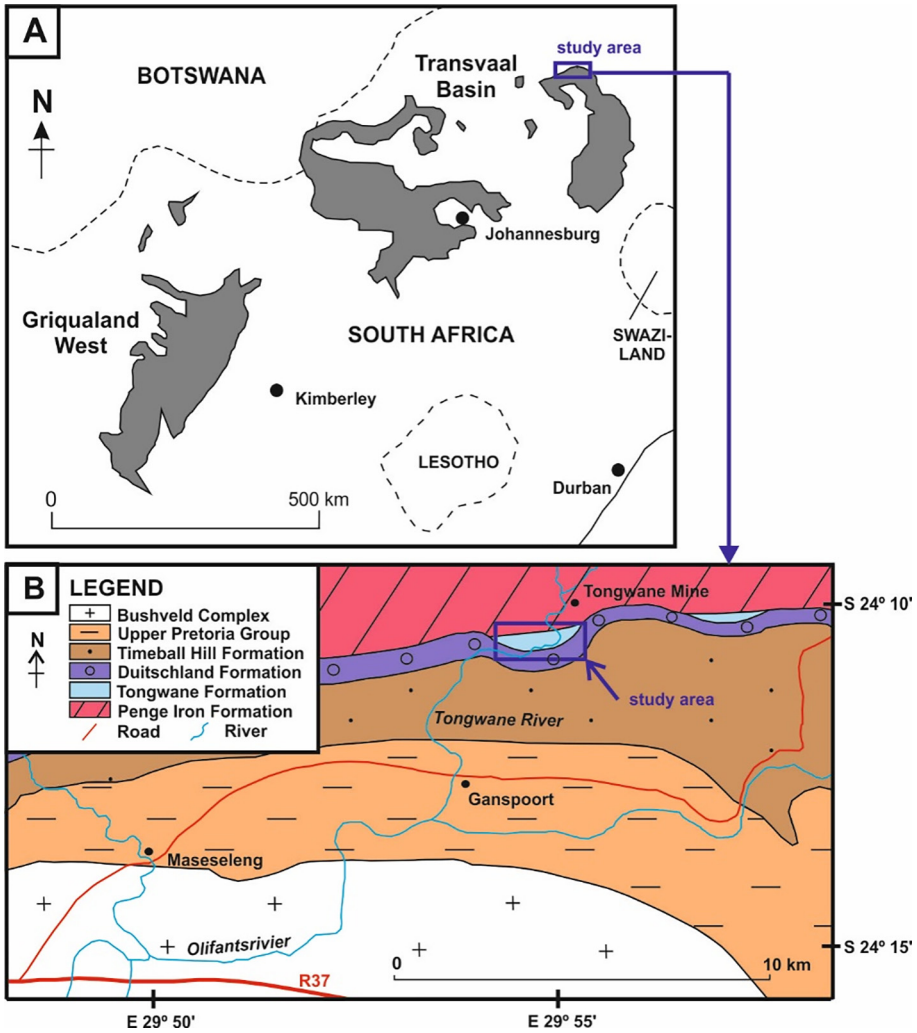

Fig. 2. regional and localised maps of the study area: (A) regional map of central and north-eastern South Africa showing the Transvaal and Griqualand West depositional basins in which the Transvaal Supergroup is preserved; (B) location of the study area and type section of the Tongwane Formation. Modified after Schröder and Warke (2016).

2. Background

2.1. Geological setting

The Tongwane Formation (Chuniespoort Group) conformably overlies the Penge Iron Formation in the eastern Transvaal Basin and is unconformably overlain by the Duitschland Formation (Schröder and Warke, 2016; Fig. 1). The unconformity at the base of the Duitschland Formation incises deeply into the upper Chuniespoort Group; Tongwane strata are only locally preserved in the gorge of the Tongwane River (Fig. 2; Martini, 1979; Schröder and Warke, 2016).

The Tongwane Formation is a 220 m thick mixed succession of iron-formation, shales, sandstones, and dolomitic carbonates (Fig. 3) which has been separated into six distinct lithofacies (LF1-LF6; Table 1) which were deposited in a regressive cycle (Schröder and Warke, 2016). The lithofacies of the Tongwane Formation record the termination of widespread banded iron formation (BIF) deposition, and the re-establishment of carbonate deposition, in the Transvaal Basin. The middle and upper portions of the succession are dominated by a distally-steepened progradational carbonate ramp which underwent periods of platform margin collapse.

Deposition of the Tongwane Formation is constrained to between ~2480 Ma (Nelson et al. 1999) and ~2310 Ma (Hannah et al., 2004; Rasmussen et al. 2013) by the Penge and the Timeball Hill (Schröder and Warke, 2016) formations, respectively (Fig. 1). Inner ramp carbonates of the massive dolomite member (LF6) preserve hummocky cross-stratification and ripple laminations indicating deposition in shallow depths around storm to fair-weather wave-base, i.e. 10 s of m (Schröder and Warke, 2016). Detrital zircon studies suggest a maximum depositional age of 2424 ± 12 Ma for the overlying (upper) Duitschland Formation (Schröder et al., 2016). The Penge Iron Formation is robustly correlated with the Asbesheuwels Subgroup in Griqualand West where the equivalent BIF may be as young as 2440–2446 Ma (Beukes and Gutzmer, 2008), plausibly constraining the Tongwane Formation's deposition to ~2420–2440 Ma. This places the deposition of the succession in the timeframe of the GOE, immediately prior to the loss of the MIF-S signal (Guo et al., 2009; Luo et al., 2016) and temporally equivalent to other Paleoproterozoic carbonate-bearing successions, such as the aforementioned upper Koegas Subgroup and Moodraai Formation in Griqualand West and the Polisarka Formation in Fennoscandia (Brasier et al., 2013).

The Tongwane Formation has been contact metamorphosed by the intrusion of the ~8 km thick Bushveld Igneous Complex into the upper Transvaal Supergroup at ~2060 Ma (Sharpe and Chadwick, 1982; Altermann and Nelson, 1998). The peak metamorphic temperature at the Tongwane type section has not been directly evaluated by previous studies (Bekker et al., 2001; Guo et al., 2009). In the underlying Penge Iron Formation, temperatures of 340–420 °C and 420–460 °C were

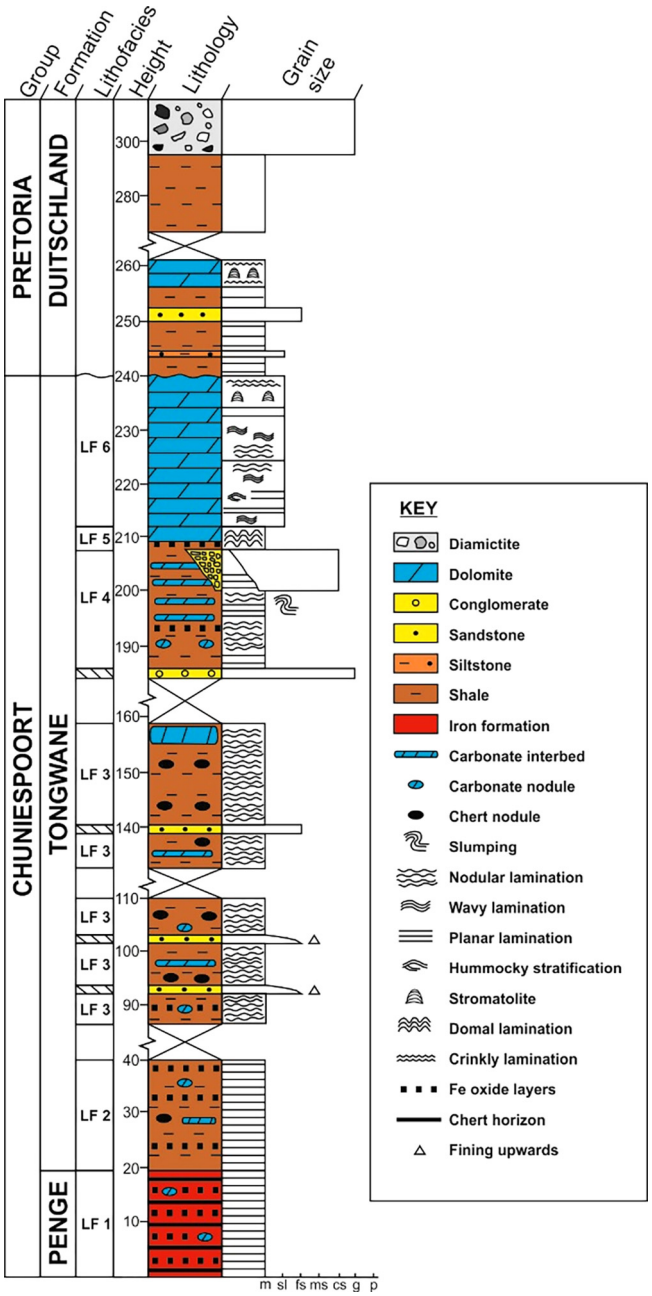

Fig. 3. sedimentary log through the Tongwane Formation as preserved at the type locality of Tongwane Gorge.

determined at the localities of Mafefe and Penge, respectively (Miyano and Beukes, 1997). As metamorphic grade increases upwards through the Transvaal Supergroup, due to increasing proximity to the base of the Bushveld intrusion (Miyano and Beukes, 1997) the metamorphic grade at Mafefe and Penge probably represents the minimum temperatures experienced by the Tongwane Formation. South of Mafefe, the 500 °C and 600 °C isotherms in the metamorphic aureole of the Bushveld intrusion undergo a swing in strike (Button, 1973, Sharpe and Chadwick, 1982); when projected westwards the Tongwane section lies between these isotherms.

2.2. Positive carbon isotope excursions and oxygen accumulation

It has been proposed that high $\delta^{13}C_{carb}$ values, i.e. > +2 $‰_{VPDB}$, reflect increased burial of ^{12}C-enriched organic matter (Veizer et al., 1992; Shields and Veizer, 2002; Prokoph et al., 2008). If organic matter is buried rapidly it escapes oxidation in the water-column by photosynthetically produced free oxygen, hence higher $\delta^{13}C_{carb}$ values can also monitor oxygen accumulation (Des Marais et al., 1992; Karhu and Holland, 1996).

In the Tongwane Formation, an unpublished study recorded $\delta^{13}C_{carb}$ values of +3.0 to +3.1 $‰_{VPDB}$ (n = 2; Swart, 1999). Subsequent studies have reported variable values of +1.9 to +3.5 $‰_{VPDB}$ (n = 5; Bekker et al., 2001) and −0.8 $‰_{VPDB}$ (n = 1; Guo et al., 2009). It has been argued that these values are evidence of increased oxygen production on the Tongwane platform, and that this may have destabilized a Paleoproterozoic greenhouse, pushing the planet into icehouse conditions (Gumsley et al., 2017). However, the total dataset from the Tongwane Formation is small (n = 6) and has not currently been discussed with respect to its depositional environment, and diagenetic and metamorphic history. These factors are important as stable carbon isotope trends also monitor $\delta^{13}C$ change over space within a basin, as well as temporal change (Frauenstein et al., 2009) and can be reset during diagenesis and contact metamorphism (Valley, 1986). Further, caution must be applied in interpreting a global, secular trend as $\delta^{13}C_{carb}$ trends can reflect localized, basin specific, processes (Frauenstein et al., 2009).

This fact is exemplified by the variable early Paleoproterozoic $\delta^{13}C_{carb}$ record in the Transvaal. Neoarchean Campbellrand-Malmani carbonates typically possess $\delta^{13}C_{carb}$ values of 0 ± 2 $‰_{VPDB}$ (Veizer et al., 1992; Shields and Veizer, 2002; Prokoph et al., 2008; Fischer et al., 2009), although these values are marginally higher in lagoonal and pertidal facies (Eroglu et al., 2017). Similar, though negative, values (−0.8 to −2.2 $‰_{VPDB}$) are noted in limestones of the Moodraai platform (Tsikos et al., 2001). Dolomites from the Moodraai Formation have slightly heavier (+0.51to +0.64$‰_{VPDB}$) $\delta^{13}C_{carb}$ values (Bau et al., 1999). Carbonates in the upper Koegas Subgroup and lower Duitschland Formation possess similar negative values of ~0 to −3 $‰_{VPDB}$ (Bekker et al., 2001; Frauenstein et al., 2009); only the upper Duitschland formation records a definitive +10 $‰_{VPDB}$ carbon stable isotope excursion (Buick et al., 1998; Bekker et al., 2001; Frauenstein et al., 2009; Guo et al., 2009).

2.3. Cerium anomalies

Rare earth element (REE) and yttrium (Y) trends, normalized to Post Archean Australian Shale (PAAS; Taylor and McLennan, 1985), can be used to evaluate whether a marine signal has been preserved in ancient carbonates and herein are denoted 'REY_{SN}'. Marine REY_{SN} patterns show: (i) positive anomalies of La_{SN} and Gd_{SN} (Bau and Dulski, 1996), (ii) elevated Y/Ho ratios of ~40–90 (Van Kranendonk et al., 2003; Allwood et al., 2010), and (iii) light REE (LREE) depletion relative to heavy REE (HREE), as monitored by either Nd_{SN}/Yb_{SN} ratios < 1 (Van Kranendonk et al., 2003) or Pr_{SN}/Yb_{SN} < 1 (Lawrence et al., 2006).

Unlike the other REEs, anomalies of Eu_{SN} and Ce_{SN} are redox dependent. During the Neoarchean and early Paleoproterozoic an increased hydrothermal component within seawater causes a positive Eu_{SN} anomaly that is commonly recorded in carbonates (Beukes and Gutzmer, 2008). Negative Ce_{SN} anomalies are produced when soluble Ce^{3+} is oxidized to insoluble Ce^{4+} following sorption onto Mn- and Fe-oxyhydroxide surfaces in environments with a sufficient levels of oxygen (Bau and Dulski, 1996; Bau, 1999; Bau and Koschinsky, 2009). The resulting Ce-depleted seawater signal is then incorporated into carbonates upon their precipitation. Positive Ce_{SN} anomalies are produced where cerium oxidation proceeds as above, but sinking particulate Mn and Fe-oxyhydroxides are reduced at a redoxcline, which also reduces and releases the adsorbed cerium (Tostevin et al., 2016b). This shuttles Ce^{3+} into a pool at the redoxcline where cerium is present in higher concentrations that the other redox insensitive REEs; carbonates that precipitate from this pool therefore carry a positive Ce_{SN} anomaly (Tostevin et al., 2016b). Therefore, the identification of cerium anomalies is a powerful technique for probing shallow water

Table 1
lithofacies assemblages constituting the Tongwane Formation, after Schröder and Warke (2016).

LF	Lithology & Height	Field description	Microfacies	Mineralogy	Interpretation & depositional environment
1	BIF (0–20 m)	Fe oxides, chert, siderite horizons alternate in dm- to cm-scale interbeds with minor, cm-, siderite/sideritic chert nodules. Finely laminated	mm-scale alternation of chert and Fe-oxides, the latter partially replaced by tabular to acicular riebeckite (~500–μm long axis)	Chert, quartz, magnetite, riebeckite	Hydrothermal source of Fe. Contact metamorphic overprint. Deposition below SWB
2	Shale (20–40 m)	Dark grey to black unit with thin, tabular beds. Minor cm-thick interbeds and nodules of ferruginous dolomite and chert	n.d.	Chert, dolomite, calcite, grunerite, riebeckite, magnetite, biotite; see also Table 4.3	Deposition below SWB
3	Siliceous mudstone with nodular carbonate (40–160 m)	Thickly to thinly bedded, strongly silicified mudstone with mm to cm scale nodules, and nodular interbeds, of dolomite. Alternating chert, ankerite, Fe-oxide and riebeckite laminae	Fine, angular, detrital quartz in mm-thick laminae. Also clay minerals and biotite; grunerite obscures microtextures	Quartz, biotite, ankerite, hematite, augite, magnetite, grunerite, goethite; see also Table 4.3	Clastic input from gravity deposits from slope. Contact metamorphic overprint. Deposition below SWB.
4	Siliceous mudstone with dolomite interbeds (185 – 208 m)	Thinly bedded shales/siliceous mudstones interbedded with thin bands (> 10 cm wide, ~1cm thick) and pre-compactional nodules (average diameter 3–5 cm) of dolomite. Yellow-brown weathering dolomite comprises 20–50% of thickness, some dolomites with flat and wavy lamination and m-scale slump structures	Dolo-microspar (< 30 μm) with dissolution seams, euhedral cubic pyrite crystals and lack of clay minerals and biotite. Grunerite formation in non-carbonate facies	Chert, quartz, dolomite, biotite, magnetite, grunerite, albite, pyrochlore, chamosite, dravite; see also Table 4.3	Increasing carbonate export and/or in-situ precipitation. Gravity-driven processes and slope margin collapse. Deposition below SWB on slope
5	Dolomite with siliciclastic mudstone interbeds (208–212 m)	Thickly to thinly bedded, ~60% cm- and dm-thick dolomite beds. Domal fabric. Siliceous mudstone up to 20 cm thick prominent at the top of unit	Mudstone layers 10–12 mm thick, interbedded with xenotopic dolo-microspar (crystals < 30 μm; locally recrystallized < 460 μm along interface of both lithologies)	Dolomite, calcite, magnetite, biotite, chlorite, talc; see also Table 4.3	Domal fabric: stromatolites and/or slumps. Carbonate export and benthic precipitation.Gravity-driven processes. Deposition below SWB on slope
6	Massive dolomite (212–240 m)	Yellow-brown weathering, medium grey dolomite. Predominantly massive although flat to wavy lamination, hummocky cross-stratification and wave ripples (paleo-azimuths between 120° and 130° measured). Undulating bed contacts and minor mudstone seams. Crinkly and domal lamination. Chert nodule frequency increases upward	Xenotopic dolomite (crystals < 100 μm); stylolites are often overprinted by euhedral pyrite	Quartz, dolomite, calcite, biotite, clinochlore, huntite, dravite ± albite, rutile, orthoclase, pyrite muscovite, birnessite; see also Table 4.3	Shallowing upwards from SWB to above FWWB: mid to inner ramp

oxygenation. There has been little prior evaluation of Ce_{SN} anomalies in Transvaal carbonates with no currently published data from the Campbellrand, Malmani, and Koegas subgroups or the Tongwane Formation. Carbonates of the Moodraai Formation do not record any Ce_{SN} anomalies (Bau et al., 1999).

At first, anomalies of Gd_{SN}, La_{SN}, Ce_{SN}, Pr_{SN} and Eu_{SN} were calculated on the assumption that the concentration difference between neighboring pairs remains constant (Table S1; Bau and Dulski, 1996). However, using this calculation, the over-abundance of La in seawater can often produce an artificial negative Ce_{SN} anomaly (Lawrence and Kamber, 2006; 2007), however true La_{SN} and Ce_{SN} anomalies can be graphically distinguished (Bau and Dulski, 1996). Alternatively, it can be assumed that the ratio of concentrations between neighboring pairs is constant (Lawrence and Kamber, 2006; 2007; Lawrence et al., 2006). These equations do not utilize La and so allow for the detection of true negative Ce_{SN} anomalies without the need for a graph (Lawrence and Kamber, 2006; 2007; Kamber et al., 2014). This method is being increasingly applied by studies on ancient carbonates (e.g. Tang et al., 2016, Tostevin et al., 2016a,b). However, Ce concentrations predicted using the Lawrence et al. (2006) method can be anomalously low, leading to artificial positive Ce_{SN} anomalies of up to 20% (Kamber et al., 2014). As this method has not been widely used in the calculation of Ce anomalies in pre-GOE successions both calculation methods are used here.

3. Methods

Carbonate samples from a range of lithofacies were collected from the type section at Tongwane Gorge (Schröder and Warke, 2016). Powders extracted for stable isotope (> 5 mg) and trace element analysis (30–100 mg) were microdrilled from the samples to avoid veining and areas of alteration or weathering. Petrographic methods included transmitted, reflected light and cathodoluminescence microscopy. Cathodoluminescence microscopy was conducted at the University of Manchester with a Citl 8200 Mark 2 cold-cathodoluminescence machine, using a vacuum of ~0.2 Torr, a cathode current of 310-335 μA and an accelerating voltage of 10–12 kV. X-ray diffraction (XRD) analyses were conducted at the Williamson Research Centre at the University of Manchester using a Bruker D8 Advance Diffractometer (Cu Kα X-ray source). Samples were scanned from 5 to 70° 2θ using a step size of 0.02° and a counting time of 0.2 s per step.

Inductively Coupled Plasma Mass Spectrometry (ICP-MS) and Inductively Coupled Plasma Atomic Emission Spectroscopy (ICP-AES) were conducted at the Williamson Research Centre at the University of Manchester using an Agilent 7500cx Inductively Coupled Plasma Mass Spectrometer and a Perkin-Elmer Optima 5300 dual view Inductively Coupled Plasma Atomic Emission Spectrometer, respectively. Samples of a known weight (typically 30–60 mg) were digested in 5 ml of 6 M $HCl_{(aq)}$ for 24 h. They were then diluted with 5 ml of de-ionised water (18.2 Ω) and digested a further 24 h. The samples were then microwaved at 50 °C for one hour to promote further dissolution, diluted with 10 ml of de-ionised water (18.2 Ω), and centrifuged for 10 min. Following centrifuging 5 ml of supernatant was extracted and diluted with 10 ml of de-ionized water (18.2 Ω). Samples were analyzed in batches of 46–50; four procedural blanks (per batch) were run to check for contamination of, or leaching from, the centrifuge tubes. Accuracy and precision were determined from a calcite standard of known concentration at 1, 5, 10, 50 and 100 ppb. From standard measurements, the accuracy and precision of all trace element data were better than 10.9% and 4.1% respectively with the exception of Mg, which has an accuracy and precision of 14.2% and 5.2%. For REY data accuracy and precision were better than 3.0% and 3.3% respectively; the accuracy and precision for Th and Ti were better than 6.0% and 11.7% respectively. The%RSD values for all analyses were < 9%, but typically < 5%. All raw data concentrations were corrected for dilution and the original sample weight. Concentrations which are normalized to PAAS (Taylor and McLennan, 1985) and chondrite concentrations (Anders and Grevasse, 1989) are denoted with the subscript "SN" and "CN" respectively, e.g. La_{SN}, La_{CN}.

Stable isotope analysis was performed on drilled carbonate phases at the Geologisches-Paläontologisches Institut, Westfälische Wilhelms-Universität, Münster using an automated on-line-system attached to a ThermoElemental Delta Plus XL mass spectrometer. For carbonate $\delta^{13}C$ and $\delta^{18}O$ measurements, CO_2 was liberated via phosphorylation at 75 °C (Wachter and Hayes, 1985). Results are expressed in the standard delta notation as per mil differences to the V-PDB standard ($‰_{VPDB}$).

4. Results

4.1. Petrographic observations: Cathodoluminescence and XRD

The sedimentological microfacies of the Tongwane Formation record a shallowing-upward trend from banded iron formations (LF1) to massive dolomites deposited above wave base (LF6) (Fig. 3; Table 1; Schröder and Warke, 2016). Intermediate facies record increased siliciclastic input and export of carbonate, preserved in thin carbonate interbeds below the main carbonate unit (LF6) (Fig. 3). Bulk-rock XRD and XRF data show a parallel increase in carbonate and support this trend (Schröder and Warke, 2016).

Within the massive dolomite facies (LF6), and in one example from a dolomite interbed in LF4, dolomites preserve up to four discrete generations of zoning (D1-D4) and have not been monotonously recrystallized. Rarely preserved D1 (crystal core) zones consist of either: (i) a corroded, usually anhedral, orange luminescent center (Fig. 4A) or, (ii) a dull red to non-luminescent euhedral rhomb (Fig. 4B). Second generation (D2) textures are the most commonly observed and consist of dull-red luminescent dolomite with variable planar-e to planar-s (or hypidiotopic to idiotopic) textures (Fig. 4B; Gregg and Sibley, 1984; Friedman, 1965). Thin, yellow-orange luminescent rims which form exclusively on planar-e D2 textures constitute D3 zones (Fig. 4C). Fourth generation (D4) textures consist of non-luminescent, planar-s dolomite, which in some areas appears xenotopic (Fig. 4C). Veins of brightly orange-yellow carbonate cut through D1-D4 textures. The carbonates in the lower parts of the succession (LF2-LF4) consist of monotonously recrystallized calcite (with minor dolomite, siderite, and ankerite; Tables 1 And 3) which appear under cathodoluminescence as yellow, brightly-luminescent carbonate with no internal zoning. No distinction is seen between the dominant yellow luminescence seen in the host carbonate and that seen in carbonate veins (Fig. 4D). Carbonates from the lower succession also contain grunerite, riebeckite, and talc, the latter of which is not identified in thin section.

Microfacies description of the non-carbonate bearing lithofacies assemblages (i.e. LF1 and 2) was outlined by Schröder and Warke (2016), and is summarized in Table 1. Most pertinent to this contribution is the observation that grunerite and riebeckite are prevalent throughout the Tongwane Formation. Grunerite habit varies from bladed and acicular to partially fibrous. Grunerite rosettes are observed, however most grunerite nucleates on a clast or mineral and grows outward (Fig. 4E), commonly totally obscuring depositional and/or diagenetic textures. Riebeckite is common throughout the section but is particularly widespread within the BIF of LF1, where tabular to acicular crystals of riebeckite vary between ~500 and ~1100 μm in length. Riebeckite crystals can be seen to nucleate upon, cross-cut, and possibly pseudomorph grunerite crystals in some areas, however in most cases the timing relationships between riebeckite and grunerite are equivocal. Bladed to acicular riebeckite is also observed to nucleate upon and grow outwards from corroded hematite (Fig. 4F).

4.2. Trace and rare earth element analysis

4.2.1. Evidence for detrital contamination

Only carbonates which preserve a signal free from detrital

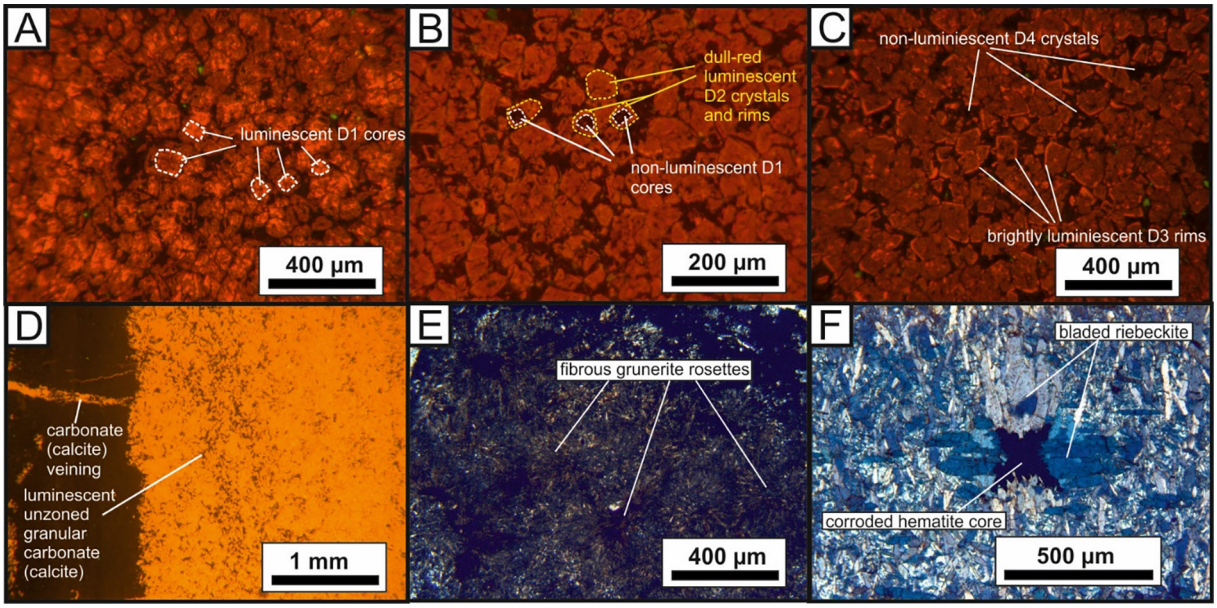

Fig. 4. (A–C): cathodoluminescence textures of dolomite, showing D1 to D4 and vein luminescence characteristics within the massive dolomite member; (D) monotonous luminescence within slope carbonates; (E) fibrous grunerite overprinting chert clasts and matrix in litharenite; (F) riebeckite crystals nucleated on and growing out from hematite in banded iron formation.

contamination are of use in evaluating marine paleoredox conditions. Detrital input can be monitored using cross plots of total REE concentration (ΣREE) against the concentrations of Al, Ti, and Th (Fig. S1). No samples show any significant correlation, suggesting that the dominant REY signal is not detrital; within the massive dolomite member (LF6) the correlations are even weaker, suggesting that a marine REY signal dominates. Additionally, REY_{SN} patterns can indicate detrital contamination where ratios of: $(La/Sm)_{CN} > 1$, $(Sm/Yb)_{SN} < 1$ and $(Eu/Sm)_{SN} > 1$ indicate no clastic contamination (Bau and Dulski, 1996). Evidence for detrital contamination using this method was seen in five samples from LF4 and LF5 (Table S3). Marine REY_{SN} patterns (see criteria in section 2.2) are noted in LF5, LF6, and one sample of LF3 (Fig. 5). All other samples have a flat signal dominated by detrital input (Fig. 5).

4.2.2. REY_{SN}: La_{SN} and Gd_{SN} anomalies, LREE depletion and Y/Ho ratios

Using the method of Bau and Dulski (1996), seven samples preserve positive La_{SN} anomalies (Fig. 6A), whereas using the method of Lawrence et al. (2006) all but two samples (in LF3 and LF4) give calculated positive La_{SN} anomalies (Fig. 6B). However, in many cases the $(La/La*)_{SN}$ ratio is very low, i.e. ~1.005–1.097. Positive anomalies of Gd_{SN} are reported in 12 samples using the Bau and Dulski (1996) method and in 14 using the Lawrence et al. (2006) method, and are not detected within three samples in LF3. LREE depletion relative to the HREE was monitored by visual inspection of REY arrays (Fig. 5) and by $(Nd/Pr)_{SN}$ and $(Pr/Yb)_{SN}$ ratios. All samples except two (LF4) show LREE depletion using these ratios. A highly irregular, non-marine REY_{SN} profile is noted in one sample from LF3. Two samples from LF6 show Y/Ho ratios > 40, consistent with fractionation in the marine realm (Allwood et al., 2010) with the other LF6 samples showing Y/Ho ratios < 40, but greater than the chondritic average Y/Ho of 25.4 ± 0.6. (Table S2; van Kranendonk et al., 2003). All samples show Y/Ho ratios which are elevated above the chondritic average, with the exception of two samples from LF4 and one from LF3.

4.2.3. Redox sensitive REY_{SN}: Eu_{SN} and Ce_{SN} anomalies

Identical, small, positive Eu_{SN} anomalies are reported using the methods of Bau and Dulski (1996) and Lawrence et al. (2006) and represent a facies-independent, seawater component which is derived from high temperature (> 250 °C) hydrothermal fluids. Positive Eu_{SN} anomalies are observed in other Neoarchean-Paleoproterozoic platform carbonates (Beukes and Gutzmer, 2008). Using the Ce_{SN} anomaly calculation of Bau and Dulski (1996) nine samples show negative Ce_{SN} anomalies where $(Pr/Pr*)_{SN} > 1$ and unity (typically < 1.1) and so caution should be applied to their interpretation. Using the Lawrence et al. (2006) method small negative Ce_{SN} anomalies are calculated in all four samples from the massive dolomite (LF6), one sample from in LF4 (which has similar petrographic and trace element characteristics to LF6 dolomites), and all three samples from LF3 (Fig. 6B).

4.3. Carbon and oxygen stable isotope results and trends

4.3.1. Carbon isotopes ($\delta^{13}C_{carb}$)

Values of $\delta^{13}C_{carb}$ range from +2.95 to −15.43 ‰$_{VPDB}$, (Fig. 7, Table 3) and show pronounced lithofacies dependence, as well as an upsection increase in the Tongwane Formation (Fig. 8). In the lowest parts of the succession, carbonate interbeds in LF2 and LF1 have the lowest $\delta^{13}C_{carb}$ values of −15.43–−13.87 ‰$_{VPDB}$. The two samples from LF3 have $\delta^{13}C_{carb}$ values of −11.38 ‰$_{VPDB}$ and −2.33 ‰$_{VPDB}$. Carbonate interbeds and pre-compactional nodules within the siliceous mudstones of LF4 show a range of −9.54–−6.88 ‰$_{VPDB}$, whereas overlying dolomite with mudstone seams (LF5) has values of −2.62–−1.91 ‰$_{VPDB}$. Maximum values of +2.22 to +2.95 ‰$_{VPDB}$ are found in the massive dolomite member (LF6), and in one sample from LF4.

4.3.2. Oxygen isotopes ($\delta^{18}O_{carb}$)

Values of $\delta^{18}O_{carb}$ vary from −3.02 to −14.26 ‰$_{VPDB}$ (Fig. 7, Table 2). The $\delta^{18}O_{carb}$ data show an opposing, but weaker, trend to the $\delta^{13}C_{carb}$ when plotted against stratigraphic height, becoming lower moving up the section (Fig. 8). The lowest values do not occur at the very top of the succession but in the interval of 195–211 m within LF5, i.e. just below the massive dolomite member (LF6). With the exception of one LF3 sample, samples from LF2 and LF1 record the highest $\delta^{18}O_{carb}$ values which range from −4.52 and −4.31 ‰$_{VPDB}$.

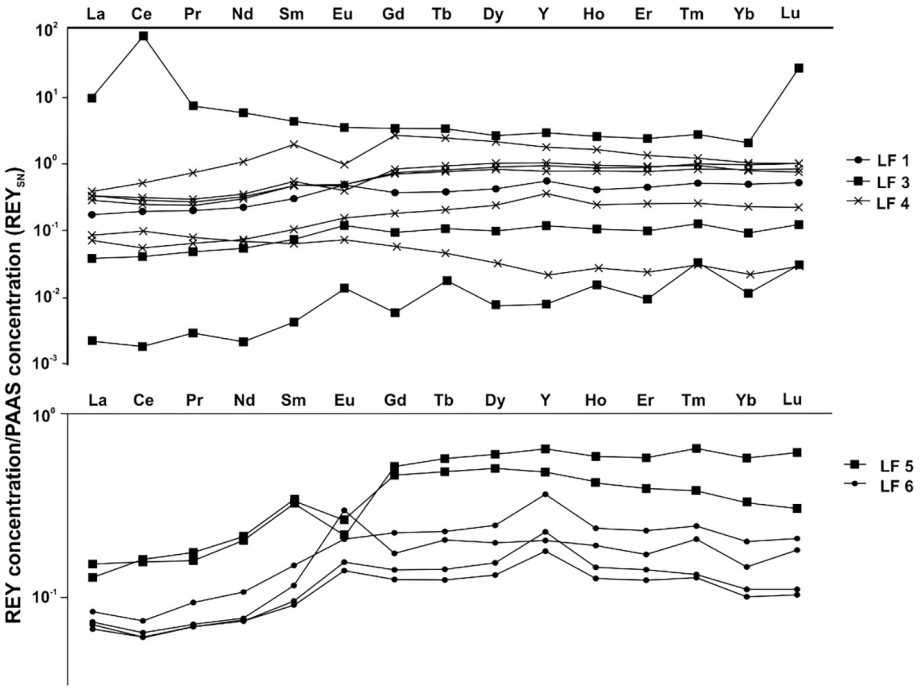

Fig. 5. REY_{SN} patterns for all six lithofacies; see text for discussion.

4.4. Trace element concentrations

Manganese concentrations vary from 945 to 10062 ppm, with two notable outliers: To42 (30 ppm) and To23 (43065 ppm; Fig. S2; 11); To23 is omitted from Fig. S3 in order to highlight the trends within the majority of the data. Within the massive dolomite member (LF6), Mn concentrations range from 3491 to 5230 ppm. Strontium concentrations range from 12.5 to 110.ppm; the lowest Sr concentrations (typically < 28 ppm) are observed within the massive dolomite member. These values are similar to Sr concentrations determined from the Tongwane and Duitschland formations by other studies (Bekker et al., 2001; Frauenstein et al., 2009). Samples with the highest concentrations of Mn generally show lower Sr concentrations (Figure S3) suggesting Mn addition and Sr loss during diagenesis (Veizer, 1983a; 1983b; Banner, 1995). Samples with low Sr (and high Mn) concentrations have $\delta^{18}O_{carb}$ values which range from −8 to −14 ‰$_{VPDB}$, however the trend is weak. No systematic relationship is observed between Mn and $\delta 13C_{carb}$; a negative correlation exists between Sr and $\delta^{13}C_{carb}$.

5. Discussion

5.1. Paragenetic history: Diagenesis and contact metamorphism

The preservation of a representative Paleoproterozoic seawater signal within the Tongwane Formation is dependent upon the absence of any overprint imparted during diagenesis and contact metamorphism from the nearby Bushveld intrusion. Petrographic observations from the carbonate and iron-rich facies elucidate the paragenetic evolution of the Tongwane Formation (Fig. 9).

5.1.1. Stage 1: Burial and diagenesis

Carbonate facies

In transmitted light dolomite appears monotonously recrystallized with planar-s textures. However, qualitative cathodoluminescence reveals four discrete generations of dolomite precipitation (D1-D4), arguing against pervasive deep burial recrystallization of Tongwane Formation carbonates and the obliteration of any shallow burial diagenetic trends (Fig. 4). The dominant generation (D2) consists of dull-red luminescent, dolomite rhombs with planar-e to planar-s textures (Sibley and Gregg, 1987), or hypidiotopic to idiotopic textures (Fig. 4) (Friedman, 1965). The preservation of planar crystal faces in planar-e D2 dolomite implies precipitation below roughening temperature, i.e. < 50–60 °C (Gregg and Sibley, 1984). Thus, assuming a geotherm of 25 °C km^{-1} (Miyashiro, 1972) and an initial formation temperature of ~20 °C, the dolomitization responsible for D2 likely occurred within the first 1–2 km of burial. Compaction caused by progressive burial gradually destroyed the pore space required for the growth of planar, euhedral faces, thus possibly restricting access for fluids forming the D3 rim and leading to the precipitation of D3 rims only along the lining of pore spaces (Fig. 4C). The final phase of precipitation is represented by non-planar, non-luminescent D4 textures which may represent a burial texture produced under deeper conditions with a more ferruginous (luminescence quenching) fluid. The Tongwane Formation experienced one cycle of deposition, burial (probably shallow) and erosion prior to deposition of the overlying Duitschland Formation. A second cycle of burial and renewed uplift to present-day outcrop followed. As no remnant of the pre-Duitschland overburden exists it is not possible to estimate the depth of burial during the first phase and to relate the shallow burial textures to a specific burial phase. Maximum burial conditions for the underlying iron formations are estimated to have been ~1.2 kbar, i.e. ~4.4 km, (Miyano and Klein, 1983; Miyano and Beukes, 1997) and ~ 3.2 to ~6.4 km for the overlying Duitschland Formation (Frauenstein et al., 2009). It is therefore conservatively estimated that the maximum burial of the Tongwane Formation was between ~3.0 and ~6.5 km. Bright-yellow luminescent calcite-dominated carbonates beneath the massive dolomite member are monotonously recrystallized and show no internal zoning; they are composed of the same carbonate phase as that which is present in thin veins (Fig. 4E). They are interpreted as having originally formed during shallow burial diagenesis, as they occur as pre-compactional carbonate nodules and interbeds, however the timing of recrystallization is unconstrained.

Ferruginous facies. Sub-greenschist grade BIF deposits (such as the Kuruman Iron Formation in Griqualand West) are dominated by chert, hematite, magnetite, siderite, ankerite, and other iron silicate phases

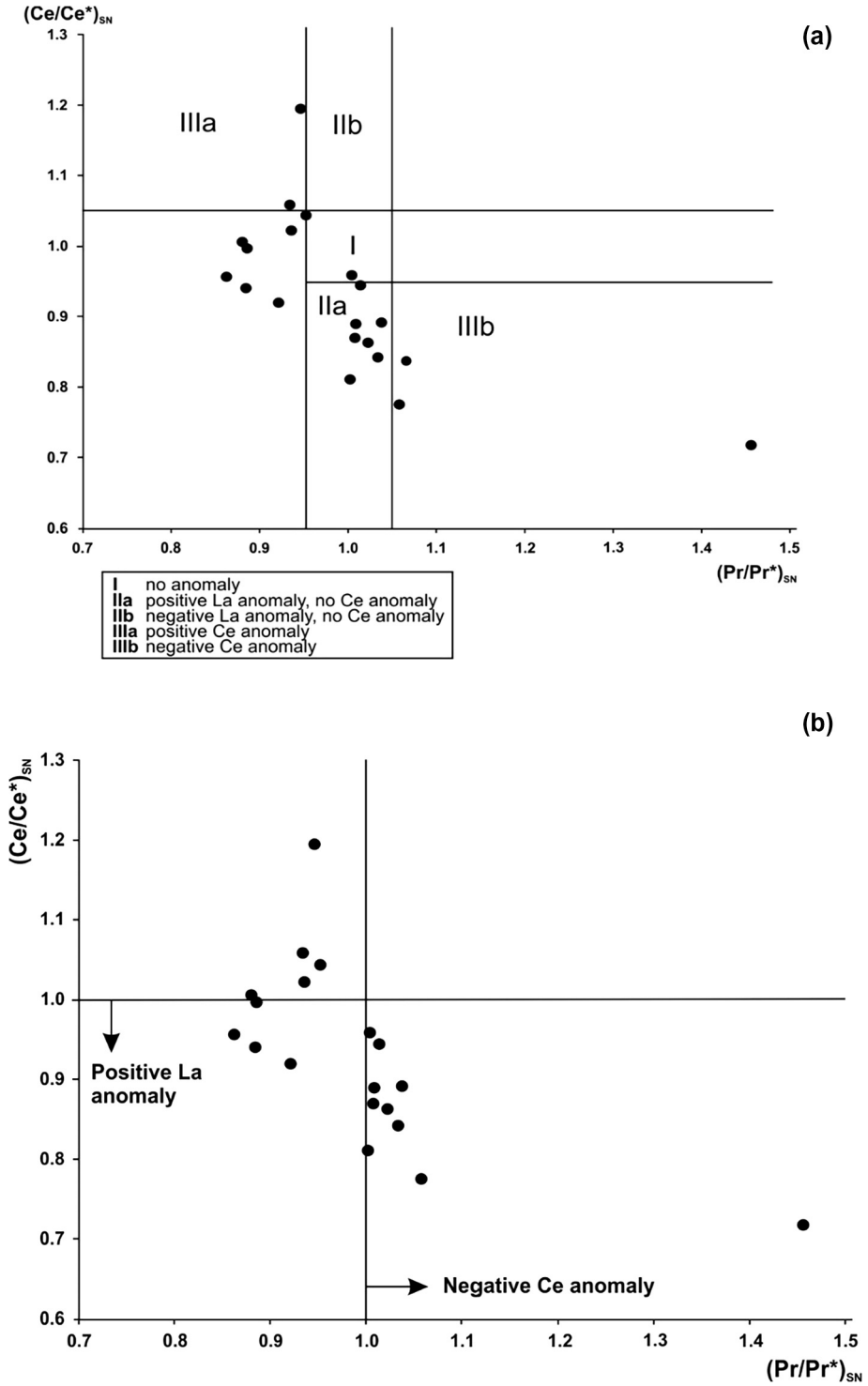

Fig. 6. A: $(Ce/Ce^*)_{SN}$ plotted against $(Pr/Pr^*)_{SN}$ enabling the graphical distinction of true negative Ce_{SN} anomalies from positive La_{SN} anomalies using the Bau and Dulski (1996) method. See text for discussion of the significance of negative Ce_{SN} anomalies. B: Ce_{SN} anomalies determined using the Lawrence et al. (2006) method plotted against La_{SN} anomalies. Most samples which show a small negative Ce_{SN} anomaly also show positive La_{SN} anomalies.

(Beukes, 1980, 1984; Beukes and Klein, 1990; Klein, 1983, 2005). These phases are produced by the reduction of precursor minerals, such as ferric oxyhydroxides, amorphous silica, siderite, and greenalite (Klein, 2005; Posth et al., 2013; Tosca et al., 2016), by reducing agents, such as organic carbon (Posth et al., 2013), during shallow burial diagenesis.

The diagenetic assemblage of the Tongwane Formation BIF (as in the Penge IF) has been altered by contact metamorphism (Miyano and Beukes, 1997), obscuring the shallow burial portion of the succession's paragenetic evolution. Experimental studies have shown that a sediment composed of ferrihydrite and glucose (simulating organic carbon) which is incubated at the burial conditions experienced by the Transvaal iron formations (i.e. 170 °C and 1.2 kbar pressure; Miyano and Klein, 1983; Miyano and Beukes, 1997) produces a resulting BIF Fe-mineral assemblage of hematite, magnetite and siderite (Posth et al., 2013). It is likely that other iron silicates such as greenalite and

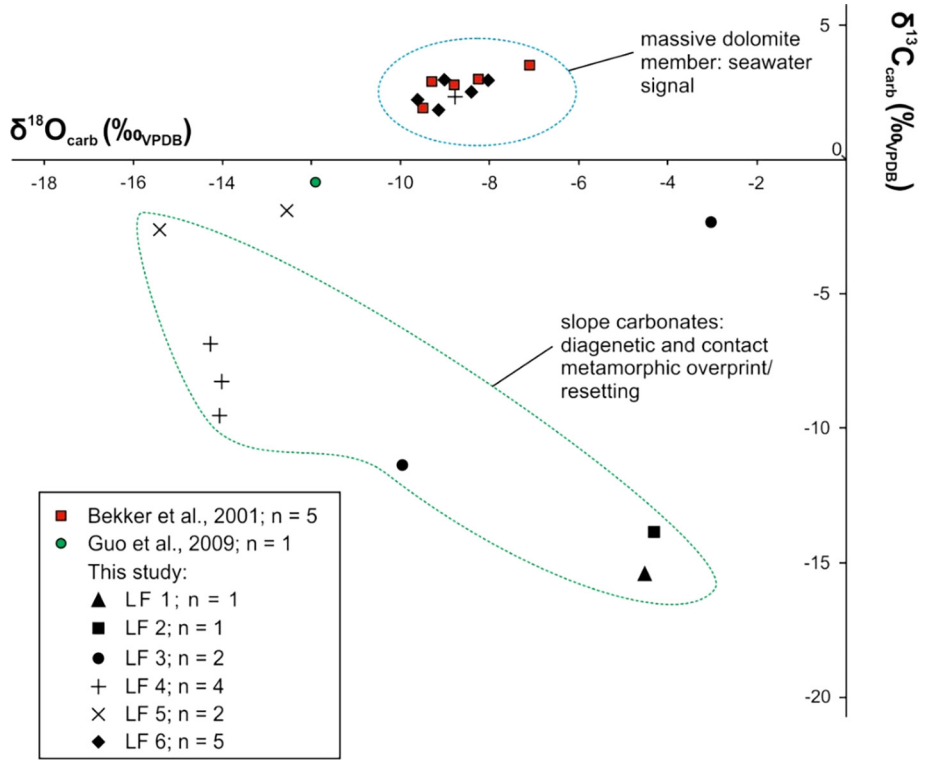

Fig. 7. $\delta^{13}C_{carb}$ and $\delta^{18}O_{carb}$ values of Tongwane Formation carbonates determined by this study and compilation of all available literature values.

minnesotaite, which are commonly observed in the correlative, sub-greenschist grade, Kuruman Iron Formation, may have been present in the shallow burial diagenetic mineral assemblage of the lower Tongwane Formation (Beukes, 1980, 1984; Beukes and Klein, 1990; Klein, 2005; Tosca et al., 2016)

Tongwane Formation BIFs, and interbedded iron-rich shales, possess a mineral assemblage of chert, magnetite, riebeckite, and grunerite with siderite only rarely detected in XRD and thin section (Tables 1 and 3; Schröder and Warke, 2016). Three possible pathways of siderite formation under the burial conditions experienced by the Transvaal iron formations are suggested by experimental work: two from the direct reduction of ferrihydrite by organic carbon, and one from the reduction of hematite induced by the thermal dehydration of iron oxyhydroxides (Posth et al., 2013). As such, siderite should be a common phase, as it is in other BIFs (Klein, 2005), however it is plausible that diagenetic siderite was removed during the contact metamorphism of the Tongwane Formation as is discussed below.

5.1.2. Stage 2: Contact metamorphism

Carbonates. An unpublished study by Swart (1999) noted one occurrence of tremolite within massive dolomites of the upper Tongwane Formation, however in this study no calc-silicate minerals were detected in thin sections or XRD analyses of the massive dolomite member (LF6). The calc-silicate mineral talc is identified in carbonate samples from LF4 and LF5, lower in the section (Table 2). While talc can form as a diagenetic calc-silicate mineral in BIF-carbonate successions like the Tongwane Formation (Tosca et al., 2010), given the temperatures experienced by the succession a metamorphic origin is more likely. Talc likely formed at temperatures up to 450–475 °C (Hover Granath et al., 1983), which is consistent with the metamorphic grade experienced at Tongwane Gorge (up to 500–600 °C; Miyano and Beukes, 1997). In addition to temperature, the formation of calc-silicate minerals in contact metamorphosed carbonate successions is dependent on silica availability. Dolomites of LF6 contain low relative bulk-rock XRF SiO_2 concentrations of less than ~10 wt% compared to carbonates lower in the succession which have bulk-rock XRF SiO_2 concentrations up to 41 wt% (Schröder and Warke, 2016). The relative paucity of calc-silicates in LF6 dolomites may therefore be the result of buffering by low silica availability.

Iron-rich facies. Within the Tongwane Formation fabric-destructive grunerite overprints depositional microtextures in a number of lithofacies (Schröder and Warke, 2016). Grunerite is a common mineral in BIF deposits that have undergone medium grade metamorphism (Klein, 2005), and can form by several pathways during the contact metamorphism of BIF. Firstly, grunerite may form by reaction of iron-rich carbonates with quartz (Klein, 2005):

$$8(Fe,Mg)CO_3 + 8SiO_2 + H_2O \rightarrow (Fe,Mg)_7Si_8O_{22}(OH)_2 + 7CO_2 \quad (R1)$$

$$7Ca(Fe,Mg)(CO_3)_2 + 8SiO_2 + H_2O \rightarrow (Fe,Mg)_7Si_8O_{22}(OH)_2 + 7CaCO_3 + 7CO_2 \quad (R2)$$

This reaction yields one mole of grunerite to every eight moles of siderite and can be sufficient to remove all the pre-existing diagenetic carbonate in a sample (Klein, 2005), as is observed in the underlying Penge Iron Formation (Miyano and Beukes, 1997). Secondly, grunerite can also form from the reaction of magnetite with iron carbonates and silica (Miyano and Beukes, 1997):

$$Fe_3O_4 + SiO_2 + (Fe,Mg)CO_3 + H_2O \rightarrow (Fe,Mg)_7Si_8O_{22}(OH)_2 + CO_2 + O_2 \quad (R3)$$

$$Fe_3O_4 + SiO_2 + Ca(Fe,Mg)(CO_3)_2 + H_2O \rightarrow (Fe,Mg)_7Si_8O_{22}(OH)_2 + CO_2 + O_2 + CaCO_3 \quad (R4)$$

The dehydration of silicate phases such as stilpnomelane and ferri-annite, which are formed during the diagenesis of BIF, can also produce grunerite in addition to biotite and chlorite (Miyano and Beukes, 1997; Klein, 2005). Stilpnomelane and ferri-annite were not detected within the BIF beds of LF1. However, it is plausible that phases such as stilpnomelane were stable at lower grades but became unstable with increasing temperature, leading to the formation of grunerite, chlorite, and biotite. Biotite and grunerite are seen in the BIF lithologies, while

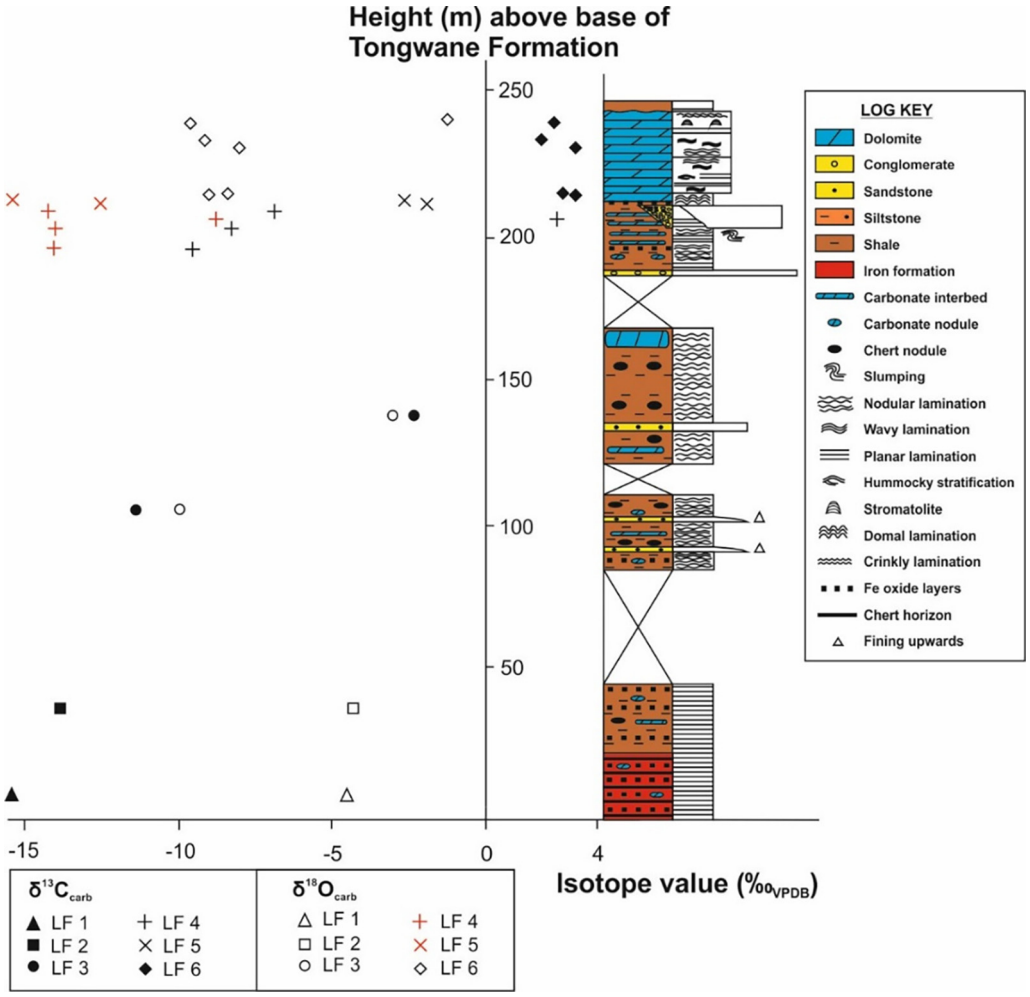

Fig. 8. $\delta^{13}C_{carb}$ and $\delta^{18}O_{carb}$ values from this study plotted against stratigraphic height. Symbols for lithofacies specific $\delta^{13}C_{carb}$ and $\delta^{18}O_{carb}$ values are shown in the key (bottom left).

Table 2
mineral assemblages determined using bulk-rock XRD.

Sample	Height (m)	Lithofacies	Phases identified
To 39	35	LF 2	Quartz, calcite, grunerite, riebeckite, magnetite, biotite
To 41	104	LF 3	Quartz, calcite, ankerite, siderite, grunerite, riebeckite, magnetite, biotite
To 43	211	LF 5	Calcite, dolomite, magnetite, biotite, clinochlore, talc
To 44	209.5	LF 5	Calcite, biotite, clinochlore, talc
To 45	205	LF 4	Calcite, riebeckite, biotite, clinochlore, talc
To 47	202	LF 4	Quartz, calcite, dolomite, riebeckite, hematite, microcline, biotite, clinochlore, talc
To 48	195	LF 4	Quartz, calcite, riebeckite, hematite, biotite, clinochlore, talc

clinochlore is detected throughout the succession (Schröder and Warke, 2016), thus any one of the above reactions may have served as a way to remove siderite from the lower Tongwane Formation.

5.1.3. Stage 3: Riebeckite formation

Riebeckite ($Na_2Fe_3^{2+}Fe_2^{3+}Si_8O_{22}(OH)_2$) can constitute up to 75 vol % of horizons within LF1 (Schröder and Warke, 2016) and is detected in LF2 to LF5, but not LF6 dolomites. Three riebeckite formation reactions are considered the most important (Miyano and Klein, 1983):

$$Na^+ + K^+ + \text{iron–oxides} + \text{quartz} + H_2O \rightarrow \text{riebeckite} \quad (R5)$$

$$Na^+ + K^+ + \text{siderite} + \text{quartz} + H_2O \rightarrow \text{riebeckite} + CO_2 \quad (R6)$$

$$Na^+ + K^+ + \text{iron–oxides} + \text{siderite} + \text{quartz} + H_2O \rightarrow \text{riebeckite} + CO_2 \quad (R7)$$

where R5 and R7 can proceed with magnetite or hematite (or both); textural evidence for reaction R5 is seen in thin section (Fig. 4F). Riebeckite can also form from grunerite (Miyano and Beukes, 1997):

$$10Fe_7Si_8O_{22}(OH)_2 + 32SiO_2 + 18H_2O + 7O_2 + 28Na^+ \rightarrow 14Na_2Fe_2^{3+}Fe_3^{2+}Si_8O_{22}(OH)_2 + 28H^+ \quad (R8)$$

This reaction is reversible, allowing for the possibility of either prograde or retrograde riebeckite formation. In the Penge Iron Formation most riebeckite is prograde and formed during burial diagenesis; its occurrence is stratigraphically controlled by the Na content of the original sediment (Miyano and Beukes, 1997). In the Tongwane Formation retrograde riebeckite can be seen cross-cutting and replacing grunerite, however, in most cases the timing relationships between riebeckite and grunerite are equivocal, and therefore both prograde and retrograde riebeckite are permissible (Fig. 9). Retrograde riebeckite has also been noted within the Penge Iron Formation, although the sodium source was not commented on (Miyano and Beukes, 1997). A late tourmaline overprint within the Penge Iron Formation has been attributed to fluids related to the intrusion of diabase sills (Miyano and Beukes, 1997). A similar late overprint of dravite, a sodium-magnesium

Table 3
ICP-MS derived trace element concentrations and stable isotope values of Tongwane Formation carbonates. Lithofacies criteria are defined in Table 4.2 and are shown in Figure 4.3.

Sample	Height (m)	Lithofacies	Mn (ppm)	Mg (%)	Ca (%)	Fe (%)	Al ppm)	Sr (ppm)	Th (ppb)	Ti (ppm)	$\delta^{13}C_{carb}$ ‰$_{VPDB}$	$\delta^{18}O_{carb}$ ‰$_{VPDB}$
To 2	205	LF 4	3703	7.55	15.05	4.82	13,145	12	2233	758	2.33	−8.78
To 3	233	LF 6	4280	8.26	18.74	2.80	3701	18	1243	342	1.83	−9.14
To 4	208	LF 4	n.d	n.d	n.d	n.d	n.d	n.d	n.d	n.d	−6.88	−14.26
To 6	212	LF 5	n.d	n.d	n.d	n.d	n.d	n.d	n.d	n.d	−2.62	−15.4
To 9	214	LF 6	3702	8.96	21.63	1.76	1916	28	641	107	2.95	−9.01
To 10	214.2	LF 6	n.d	n.d	n.d	n.d	n.d	n.d	n.d	n.d	2.51	−8.41
To 12	230	LF 6	3491	9.03	20.11	1.63	2890	20	1051	244	2.94	−8.03
To 13	239	LF 6	5230	8.27	19.23	2.44	6229	27	1027	201	2.22	−9.61
To 23	137	LF 3	43,066	1.76	4.57	9.49	3860	75	509	464	−2.33	−3.02
To 38	5	LF 1	945	0.31	17.40	14.27	1086	84	91	156	−15.43	−4.52
To 39	35	LF 2	n.d	n.d	n.d	n.d	n.d	n.d	n.d	n.d	−13.87	−4.31
To 40	104	LF 3	2724	1.25	8.67	12.94	99	110	256	16	−11.38	−9.96
To 41	104	LF 3	1310	0.32	0.69	5.97	1366	16	137	67	n.d	n.d
To 43	211	LF 5	10,062	6.12	20.72	6.03	20,182	43	180	729	−1.91	−12.55
To 44	209.5	LF 5	8699	1.53	31.36	1.03	6601	83	1031	153	n.d	n.d
To 45	205	LF 4	9367	1.02	36.92	0.63	4114	71	510	52	n.d	n.d
To 46	204	LF 4	7377	3.40	23.60	3.43	19,760	49	3709	928	n.d	n.d
To 47	202	LF 4	8472	1.34	34.8	0.77	4877	79	1110	147	−8.27	−14.01
To 48	195	LF 4	7427	1.53	33.58	1.95	6568	35	1325	119	−9.54	−14.06

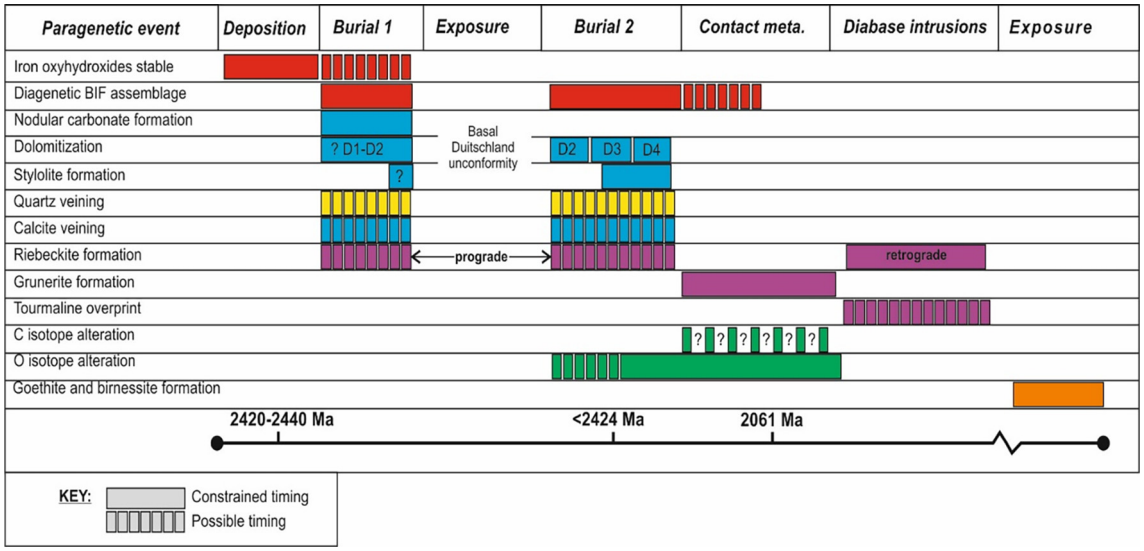

Fig. 9. proposed paragenetic evolution of the Tongwane Formation; see text for discussion.

tourmaline, is seen within portions of the Tongwane Formation (Table 1; Schröder and Warke, 2016). Possibly, the sodium-rich fluids responsible for the tourmaline overprint may also have facilitated the formation of retrograde riebeckite, however further investigation is needed. Riebeckite formation may also have removed siderite (Miyano and Klein, 1983):

$$5FeCO_3 + 8SiO_2 + 7H_2O + 2Na^+ + 1/2O_2 \rightarrow \text{riebeckite} + 5CO_3^{2-} + 12H^+ \quad \text{(R9)}$$

In the Marra Mamba Iron Formation in Western Australia, riebeckite-rich rocks are devoid of siderite (Klein and Gole, 1981). The prograde reactions of stilpnomelane with iron-oxides and carbonates to produce riebeckite (and mica) may also have formed riebeckite but are generally considered less important (Miyano and Klein, 1983).

5.1.4. Summary of the paragenetic evolution

The shallow burial diagenetic assemblages of the BIF and ferruginous shale deposits are not preserved due to the formation of fabric-destructive grunerite during contact metamorphism. Grunerite formation at increasingly higher temperatures probably removed iron-silicates and siderite from the succession. Grunerite may also have formed from prograde riebeckite, although textural evidence for retrograde riebeckite formation from grunerite is observed. Within the platform dolomites (LF6) burial dolomitization textures are preserved and have not been obliterated by recrystallization. Dolomites in LF6 do not contain calc-silicates, possibly due to low initial silica concentrations. Carbonate nodules and interbeds from below the platform are uniformly luminescent, display no zoning, are calcite-dominated and contain talc.

5.2. Evidence for retention of a Paleoproterozoic marine signal

5.2.1. Massive dolomite member (LF6)

Platform dolomites possess REY_{SN} patterns that lack detrital contamination and show marine characteristics such as positive La_{SN}, Gd_{SN} and Eu_{SN} anomalies, elevated Y/Ho ratios, and LREE depletion. Values of $\delta^{13}C_{carb}$ fall in the range +1.83–+2.95 ‰$_{VPDB}$, which is broadly

typical of Paleoproterozoic seawater (Veizer et al., 1992; Shields and Veizer, 2002; Prokoph et al., 2008).

Petrographic observations indicate that LF6 dolomites have experienced several generations of dolomitization. The dominant planar-e to planar-s D2 generation likely formed below roughening temperature and therefore could have formed within the first ~1–2 km of burial. Planar-e D1 rhombs, which constitute the earliest dolomite generation, are only rarely preserved. Later generations of dolomite (e.g. D4) may have formed during deeper burial, however cathodoluminescence textures imply that no widespread recrystallization of the LF6 dolomites occurred. Therefore, LF6 records the REY_{SN} and stable isotope characteristics of dolomites which formed during shallow burial. Hence, any marine signal retained from the original carbonate could have survived dolomitization, burial diagenesis, and contact metamorphism.

The extent to which primary carbon and oxygen isotopic values, and REY_{SN} patterns, are affected by dolomitization depends on the nature of the dolomitizing fluid (van Kranendonk et al., 2003). During diagenesis and dolomitization water to rock ratios of $> 10^3$ are required to alter REY_{SN} patterns and $\delta^{13}C_{carb}$ values, but smaller ratios ($<1\,0^1$) can alter $\delta^{18}O_{carb}$ values (Banner and Hanson, 1990). Primary REY_{SN} patterns can be preserved through multiple stages of dolomitization, including early burial dolomitization, where the fluids are similar in composition to seawater (Banner et al., 1988). However, when dolomitizing fluids are significantly different in composition to seawater REY_{SN} patterns can be reset (Nothdurft et al., 2004). Low $\delta^{18}O_{carb}$ values (-9.61–-8.03 ‰$_{VPDB}$) and low Sr concentrations coupled with high Mn concentrations (Fig. 8) suggest some recrystallization during deep burial (Veizer, 1983); this may cause the D3 and D4 textures. Therefore, while some recrystallization and fluid interaction may have occurred during burial it did not cause total recrystallization (and obliteration) of predominant (D2) shallow burial textures and their associated $\delta^{13}C_{carb}$ values and REY_{SN} patterns.

As in burial diagenesis, REY_{SN} patterns are only affected during metamorphism and metasomatism where associated fluids possess fluid to rock ratios $> 10^3$ (Bau, 1991). Stable isotopes (particularly oxygen) are more sensitive to resetting during contact metamorphism as they can be altered at lower fluid to rock ratios (Valley, 1986; Buick et al., 1998).

Within shallow marine carbonates of the Duitschland Formation a systematic lowering of $\delta^{18}O_{carb}$ and $\delta^{13}C_{carb}$ values with increasing proximity to the Bushveld Igneous Complex is observed (Frauenstein et al., 2009). This trend is common in contact metamorphic aureoles that form in carbonate host rocks as devolatilization reactions deplete the $\delta^{13}C_{carb}$ and $\delta^{18}O_{carb}$ values of the carbonate during the production of calc-silicate minerals and the expulsion of isotopically heavy CO_2 (Valley, 1986; Baumgartner and Valley, 2001).

Stable carbon isotopes in carbonates are often more resistant than oxygen isotopes to metamorphic resetting as the carbon is rock buffered during devolatization (Valley, 1986). Within LF6 – which retains seawater-like REY_{SN} patterns – carbon isotopes are consistent with marine values, but oxygen isotopes are 1–2‰ lower than expected. There is no petrographic evidence of calc-silicate formation within the massive dolomite member except one unsubstantiated example of tremolite reported by Swart (1999). Together, these observations suggest minimal overprinting due to contact metamorphism has occurred.

Values of $\delta^{13}C_{carb}$ from the Tongwane Formation are lowest in carbonates with high bulk rock SiO_2 concentrations (up to 40 wt%) and highest in the massive dolomite member where bulk rock SiO_2 concentrations are $<$ 1.7 wt% (Schröder and Warke, 2016). Therefore, it is possible calc-silicate formation, and associated devolatilization of CO_2 rich fluids, may have been buffered by low silica contents. It is proposed this led to the retention of a marine $\delta^{13}C_{carb}$ signal in LF6, despite the temperatures experienced. The retention of primary $\delta^{13}C_{carb}$ values in metamorphosed Paleoproterozoic carbonate successions is inferred elsewhere: e.g. in Scotland (Baker and Fallick, 1989a; Kerr et al., 2016), Norway (Baker and Fallick, 1989b), Canada (Ghent and O'Neil, 1985), and Australia (McNaughton and Wilson, 1983).

5.2.2. The lower carbonates (LF1-5)

The carbonates beneath the massive dolomite member do not show seawater-like REY_{SN} patterns and anomalies. These carbonates lack any of the D1 to D4 textures observed in the massive dolomite and are monotonously recrystallized and show genetic relationships to vein fills. Values of $\delta^{13}C_{carb}$ and $\delta^{18}O_{carb}$ are significantly lower and several calcite dominated carbonates from LF4 and LF5 contain the calc-silicate mineral talc (Table 2).

This systematic decrease in $\delta^{13}C_{carb}$ values moving down the section mainly is interpreted as reflecting an increased generation and circulation of H_2O and CO_2 rich devolatilization fluids during contact metamorphism. This hypothesis is supported by the occurrence of talc in several samples from LF4 and 5 (Table 2), higher bulk-rock silica concentrations in the lower carbonates (Schröder and Warke, 2016), and the strong relationship between silica concentration and $\delta^{13}C_{carb}$ values. Unlike in LF6, as discussed above, higher relative silica concentrations in the lower carbonates did not restrict devolatization reactions.

Therefore, it is probable that contact metamorphism also caused lowering of $\delta^{18}O_{carb}$ values. However, highly altered $\delta^{18}O_{carb}$ values often occur in lower carbonates with higher Sr concentrations, possibly suggesting addition of radiogenic Sr which may have occurred during burial diagenesis. Thus, the $\delta^{18}O_{carb}$ values of LF1-5 carbonates may reflect a combination of contact metamorphism and burial diagenesis.

Given the flat REY_{SN} profiles observed, and REE ratios indicative of detrital contamination, LF1-5 carbonate nodules and interbeds may not have initially recorded a marine signal at all, regardless of whether or not any signal has been altered during diagenesis and metamorphism.

5.3. Implications for ocean redox and global paleoclimate change

The Tongwane Formation rests conformably on the Penge Iron Formation. It records the reestablishment of shallow-water carbonate production and the termination of widespread BIF deposition in the eastern Transvaal Basin during the early Paleoproterozoic rise in oxygen. It immediately precedes the loss of the MIF-S signal in the overlying Duitschland and Rooihoogte formations (Guo et al., 2009; Luo et al., 2016). Due to recent stratigraphic revisions by Gumsley et al. (2017) the Tongwane Formation is broadly contemporaneous with the Postmasburg Group including its record of: (i) the severe glaciation recorded in the Makganyene Formation, (ii) manganese oxidation in the Hotazel Formation, (iii) and shallow water carbonate deposition in the Moodraai Formation. However, as the Tongwane Formation conformably overlies the Penge Iron Formation its stratigraphic position implies that the Tongwane Formation predates these major paleoenvironmental changes and that the platform carbonates (LF6) of the Tongwane Formation could provide an earlier archive of marine paleoredox conditions on the eve of the GOE.

5.3.1. Evidence for a positive carbon isotope excursion in the Tongwane Formation

It has been proposed that assembly of the low-latitude supercontinent 'Superia' was accompanied by the extrusion of several large igneous provinces (LIP), across the Kaapvaal, Pilbara, Wyoming, Hearne, Kola-Karelia and Superior cratons which are dated to ~2.4 Ga (Gumsley et al., 2017). Weathering of these LIPs may have enhanced CO_2 drawdown and caused a flux of primary productivity limiting nutrients into shallow water environments, stimulating cyanobacterial photosynthesis and organic carbon burial, thereby enhancing oxygen production (Gumsley et al., 2017). This hypothetical rise in oxygen may have destabilised atmospheric methane, which together with enhanced CO_2 drawdown, may have collapsed the greenhouse effect and pushed the Paleoproterozoic climate into a 'snowball Earth' (Gumsley et al., 2017), which is recorded in the Makganyene Formation (Evans et al., 1997). The causal linkage of the GOE with a snowball Earth event triggered by methane oxidation has been proposed elsewhere (Pavlov

and Kasting, 2002; Kopp et al., 2005; Brasier et al., 2013).

Oxygen accumulation prior to the glaciation has been suggested on the basis of $\delta^{13}C_{carb}$ values of up to +3.5 ‰$_{VPDB}$ in the Tongwane Formation (Bekker et al., 2001; Gumsley et al., 2017). Methane oxidation may be supported by low $\delta^{13}C_{carb}$ values (−5–0 ‰$_{VPDB}$) from shallow water carbonates of the Polisarka Formation which was deposited at a similar time to the Tongwane Formation (i.e. 2440–2430 Ma) in a similar environment (Brasier et al., 2013).

The mean $\delta^{13}C_{carb}$ value of LF6 shallow water dolomites presented in this contribution (i.e. +2.46 ‰$_{VPDB}$; n = 6) is similar to that reported Bekker et al. (2001) (i.e. + 2.8 ‰$_{VPDB}$; n = 5). Combining the two datasets with that of Guo et al. (2009) gives a mean $\delta^{13}C_{carb}$ value of +2.33 ‰$_{VPDB}$ (n = 12) for LF6 dolomites in the upper Tongwane Formation. Originally, Bekker et al. (2001) reported a larger range of $\delta^{13}C_{carb}$ values (+1.9–+3.5 ‰$_{VPDB}$) than determined here (+1.83–+2.95 ‰$_{VPDB}$) and used values > 3 ‰$_{VPDB}$ to argue for enhanced carbon burial and concomitant oxygen accumulation in the eastern Transvaal Basin during the deposition of the Tongwane Formation. However, with the additional data presented here the new average $\delta^{13}C_{carb}$ value of +2.33 ‰$_{VPDB}$ is only marginally elevated with respect to the 0 ± 2 ‰$_{VPDB}$ range of Paleoproterozoic seawater (Veizer et al., 1992; Shields and Veizer, 2002; Prokoph et al., 2008). The new data are not incompatible with enhanced carbon burial and oxygen accumulation, however the resultant mean +0.33 ‰$_{VPDB}$ excursion above the average $\delta^{13}C_{carb}$ range is not comparable in magnitude to other early Paleoproterozoic positive isotope excursions interpreted as reflecting carbon burial and oxygen accumulation, e.g. in the upper Duitschland Formation (Bekker et al., 2001; Frauenstein et al., 2009). Similarly they are much smaller than noted late Paleoproterozoic, Mesoproterozoic and Neoproterozoic positive isotope excursions which consist of $\delta^{13}C_{carb}$ values of > +3.5 ‰$_{VPDB}$, and may be as high as ~ +12 ‰$_{VPDB}$ (Karhu and Holland, 1996; Bartley and Kah, 2004).

Therefore, as there is no significant carbon isotope excursion, the upper dolomite member of the Tongwane Formation does not appear to record a pulse of organic carbon burial and oxygen accumulation. As such, the Tongwane Formation $\delta^{13}C_{carb}$ values cannot be used to argue for greenhouse destabilization through atmospheric oxygenation (Gumsley et al., 2017). Rather, Tongwane Formation $\delta^{13}C_{carb}$ values compliment other $\delta^{13}C_{carb}$ values from late Neoarchean-early Paleoproterozoic platform carbonates in the Transvaal Supergroup which fall broadly in the range of 0 ± 2 ‰$_{VPDB}$. Nonetheless, the robust temporal realignment of the Makganyene glaciation from the Rhyacian to the Siderian (Gumsley et al., 2017) brings this glaciation into the timeframe of the other Huronian glaciations (Hoffman, 2013). Conspicuously, these glaciations are broadly coeval with the GOE and a causal relationship between the two events, long proposed, may yet be proved (Kopp et al., 2005; Hoffman, 2013; Gumsley et al., 2017).

5.3.2. Comparison with coeval carbonate successions

As discussed above, several late Neoarchean-early Paleoproterozoic carbonate successions in the Transvaal Supergroup possess average $\delta^{13}C_{carb}$ values that fall in the range of 0 ± 2 ‰$_{VPDB}$.

These include carbonates of the Campbellrand-Malmani (Fischer et al., 2009; Eroglu et al., 2017) and Moodraai (Bau et al., 1999; Tsikos et al., 2001) platforms. The $\delta^{13}C_{carb}$ record of the Tongwane Formation is more similar to these successions than the carbonates within the lower Duitschland Formation and upper Koegas Subgroup (Frauenstein et al., 2009).

Beyond the Kaapvaal Craton, the Tongwane Formation is approximately coeval with the Polisarka Formation preserved within the Imandra-Varzuga greenstone belt in Fennoscandia (Brasier et al., 2013; Martin et al., 2013). Within the Polisarka Formation, low $\delta^{13}C_{carb}$ values are recorded exclusively by dolomite clasts found within host limestones with $\delta^{13}C_{carb}$ values close to ~0 ‰$_{VPDB}$. It was proposed that the dolomite clasts originated from dolomitized sediments, deposited in shallower environments that were subsequently reworked and transported to a deeper setting (Brasier et al., 2013). Why these shallow water dolomites should preserve such low $\delta^{13}C_{carb}$ remains unclear, however Brasier et al. (2013) proposed that the $\delta^{13}C_{carb}$ values could reflect – among other possible processes – oxidation of ^{12}C-enriched methane. If correct, such values could be interpreted as supporting evidence for the hypothesis that widespread methane oxidation may have triggered the Huronian glaciations.

However, these lower $\delta^{13}C_{carb}$ values from the Polisarka Formation stand in contrast to the values seen in the shallow water, upper Tongwane Formation; low $\delta^{13}C_{carb}$ values from the lower Tongwane Formation have been reset during contact metamorphsm and cannot be used to infer methane oxidation. These discrepancies suggest that it is possible, if not probable, that one or both successions record predominantly localised, basin-specific $\delta^{13}C_{carb}$ variations and not a global secular change in $\delta^{13}C_{carb}$ values in shallow-water carbonate environments.

5.3.3. Cerium anomalies and manganese oxidation

Using the method of Bau and Dulski (1996) true negative Ce_{SN} anomalies are defined where $(Ce/Ce*)_{SN} < 1$ and $(Pr/Pr*)_{SN} > 1$ with an uncertainty of around ~ 0.05. Thus, as the $(Pr/Pr*)_{SN}$ ratios are so close to unity, no true Ce_{SN} anomalies can be confidently defined (Fig. 6A). The apparent negative anomalies indicated by $(Ce/Ce*)_{SN}$ of 0.81 to 0.89 may be an artefact generated by overabundant La. To test this scenario, Ce_{SN} anomalies were also calculated, using the method of Lawrence et al. (2006) giving $(Ce/Ce*)_{SN}$ values of 0.91 to 0.97; these low magnitude Ce_{SN} anomalies (< 10%) are not interpreted as significant. Two unpublished negative Ce_{SN} anomalies from the Tongwane Formation, calculated using the Bau and Dulski (1996) method, were reported in an unpublished study by Swart (1999). However, $(Pr/Pr*)_{SN}$ values of 1.05–1.07, and $(Ce/Ce*)_{SN}$ values of 0.86–0.88, show these data are also ambiguous. Recalculation using the Lawrence et al. (2006) method yields small negative Ce_{SN} anomalies of 0.86–0.88. However, as details of analytical procedure are not stated and published, these findings should be viewed cautiously.

Therefore, if significant free oxygen was accumulating in the shallow water facies of the Tongwane Formation – which is disputed – it was doing so in concentrations that were insufficient to allow for the stable preservation of any (negative or positive) cerium anomaly that would indicate redox cycling. The oxidation of Ce^{3+} in the water column is thought to occur at similar minimum oxygen concentrations as that required for Mn^{2+} oxidation to Mn^{4+} (Moffett, 1994) and it physically requires adsorption to Mn and/or Fe oxyhydroxides (Bau, 1999). The lack of a Ce_{SN} anomaly may therefore signify that no manganese oxidation occurred this time, at least in this depositional environment.

However, the correlations of Gumsley et al. (2017) imply that shortly after the deposition of the Tongwane Formation widespread oxidation of manganese occurred in the Griqualand West Basin, as recorded in the Hotazel Formation (Schneiderhan et al., 2006). This may suggest that shallow water oxygen concentrations surpassed the threshold required for manganese and cerium oxidation sometime between the deposition of these two successions. However, it is noted that there are no Ce_{SN} anomalies preserved in the Moodraai Formation (Bau et al., 1999). This carbonate platform conformably overlies, and transgressed over, the Hotazel Formation (Schneiderhan et al., 2006). Thus, it may be over-simplistic to infer a unidirectional, secular change in shallow-water oxygen concentrations using the appearance and disappearance Ce_{SN} anomalies alone.

6. Conclusions

The first detailed investigation of the paragenesis of the Tongwane Formation is presented, facilitating critical interpretation of its preserved geochemical archive. Integrated trace element, stable isotope and petrographic analyses suggest that Tongwane Formation platform

dolomites retain seawater-like REY_{SN} patterns and anomalies, and positive $\delta^{13}C_{carb}$ values indicative of early Paleoproterozoic marine values. These carbonates lack Ce_{SN} anomalies. This signal has been retained through dolomitization, burial diagenesis and medium-grade contact metamorphism, where devolatilization was buffered by low bulk rock silica concentrations. In contrast to previous studies, no significant positive isotope excursion is inferred. This questions previous suggestions that a pulse of oxygen accumulation, inferred by positive $\delta^{13}C_{carb}$ values in the Tongwane Formation, may have contributed to collapse of the Paleoproterozoic greenhouse and triggered glaciation. Negative $\delta^{13}C_{carb}$ values in Tongwane slope carbonates result from resetting of isotope systems and REY_{SN} arrays during interaction with devolatilization fluids during contact metamorphism. They are not primary values and cannot be used as evidence for methane oxidation, as argued elsewhere for broadly contemporaneous successions.

Acknowledgements

MRW was supported by a NERC-studentship through the University of Manchester. SS was supported through a Strategy Grant of the Faculty of Engineering and Physical Sciences at the University of Manchester. P. Lythgoe and J. Waters are thanked for help with the ICP-MS/AES and XRD analyses respectively. The authors thank H. Tsikos and an anonymous reviewer for constructive comments which greatly improved the manuscript.

Appendix A. Supplementary data

Supplementary data associated with this article can be found, in the online version, at http://dx.doi.org/10.1016/j.precamres.2018.04.015.

References

Allwood, A.C., Kamber, B.S., Walter, M.R., Burch, I.W., Kanik, I., 2010. Trace elements record depositional history of an Early Archean stromatolitic carbonate platform. Chem. Geol. 270, 148–163.
Altermann, W., Nelson, D.R., 1998. Sedimentation rates, basin analysis and regional correlations of three Neoarchaean and Palaeoproterozoic sub-basins of the Kaapvaal craton as inferred from precise U-Pb zircon ages from volcaniclastic sediments. Sed. Geol. 120, 225–256.
Anders, E., Grevasse, N., 1989. Abundances of the elements: Meteoritic and solar. Geochim. Cosmochim. Acta 53, 197–214.
Baker, A.J., Fallick, A.E., 1989a. Evidence from Lewisian limestones for isotopically heavy carbon in two-thousand-million-year-old sea water. Nature 337, 352–354.
Baker, A.J., Fallick, A.E., 1989b. Heavy carbon in two-billion-year-old marbles from Loftoten-Vesteralen, Norway: implications for the precambrian carbon cycle. Geochim. Cosmochim. Acta 53, 111–115.
Banner, J.L., 1995. Application of the trace element and isotope geochemistry of strontium to studies of carbonate diagenesis. Sedimentology 42, 805–824.
Banner, J.L., Hanson, G.N., 1990. Calculation of simultaneous isotopic and trace element variations during water-rock interaction with applications to carbonate diagenesis. Geochim. Cosmochim. Acta 54, 3123–3137.
Banner, J.L., Hanson, G.N., Meyers, W.J., 1988. Rare earth element and Nd isotopic variations in regionally extensive dolomites from the Burlington-Keokuk Formation (Mississippian): implications for REE mobility during carbonate diagenesis. J. Sediment. Petrol. 58, 415–432.
Bartley, J.K., Kah, L.C., 2004. Marine carbon reservoir, Corg-Ccarb coupling, and the evolution of the Proterozoic carbon cycle. Geology 32, 129–132.
Bau, M., 1991. Rare-earth element mobility during hydrothermal and metamorphic fluid-rock interaction and the significance of the oxidation state of europium. Chem. Geol. 93, 219–230.
Bau, M., 1999. Scavenging of dissolved yttrium and rare earths by precipitating iron oxyhydroxide: experimental evidence for Ce oxidation, Y-Ho fractionation, and lanthanide tetrad effect. Geochim. Cosmochim. Acta 63, 67–77.
Bau, M., Dulski, P., 1996. Distribution of yttrium and rare-earth elements in the Penge and Kuruman iron-formations, Transvaal Supergroup, South Africa. Precambr. Res. 79, 37–55.
Bau, M., Koschinsky, A., 2009. Oxidative scavenging of cerium on hydrous Fe oxide: evidence from the distribution of rare earth elements and yttrium between Fe oxides and Mn oxides in hydrogenetic ferromanganese crusts. Geochem. J. 43, 37–47.
Bau, M., Romer, R.L., Lüders, V., Beukes, N.J., 1999. Pb, O, and C isotopes in silicified Mooidraai dolomite (Transvaal Supergroup, South Africa): implications for the composition of Paleoproterozoic seawater and 'dating' the increase of oxygen in the Precambrian atmosphere. Earth Planet. Sci. Lett. 174, 43–57.
Baumgartner, L.P., Valley, J.W., 2001. Stable isotope transport and contact metamorphic fluid flow. Rev. Mineral. Geochem. 43, 415–467.
Bekker, A., Kaufman, A.J., Karhu, J.A., Beukes, N.J., Swart, Q.D., Coetzee, L.L., Eriksson, K.A., 2001. Chemostratigraphy of the Paleoproterozoic Duitschland Formation, South Africa: implications for coupled climate change and carbon cycling. Am. J. Sci. 301, 261–285.
Bekker, A., Holland, H.D., Wang, P.-L., Rumble III, D., Stein, H.J., Hannah, J.L., Coetzee, L.L., Beukes, N.J., 2004. Dating the rise of atmospheric oxygen. Nature 427, 117–120.
Beukes, N.J., 1980. Lithofacies and stratigraphy of the Kuruman and Griquatown iron-formations, northern Cape Province, South Africa. Trans. Geol. Soc. South Africa 83, 69–86.
Beukes, N.J., 1984. Sedimentology of the Kuruman and Griquatown iron-formations, transvaal supergroup, Griqualand West, South Africa. Precambr. Res. 24, 47–84.
Beukes, N.J., Gutzmer, J., 2008. Origin and paleoenvironmental significance of major iron formations at the Archean-Paleoproterozoic boundary. Rev. Econ. Geol. 15, 5–47.
Beukes, N.J., Klein, C., 1990. Geochemistry and sedimentology of a facies transition—-from microbanded to granular iron-formation—in the early Proterozoic Transvaal Supergroup, South Africa. Precambr. Res. 47, 99–139.
Brasier, A.T., Martin, A.P., Melezhik, V.A., Prave, A.R., Condon, D.J., Fallick, A.E., Scientists, F.D., 2013. Earth's earliest global glaciation? Carbonate geochemistry and geochronology of the Polisarka Sedimentary Formation, Kola Peninsula, Russia. Precambr. Res. 235, 278–294.
Buick, I.S., Uken, R., Gibson, R.L., Wallmach, T., 1998. High-$\delta^{13}C$ Paleoproterozoic carbonates from the transvaal supergroup, South Africa. Geology 26, 875–878.
Button, A., 1973. A study of the stratigraphy and development of the Transvaal Basin in the eastern and northeastern Transvaal. PhD. thesis (unpublished). University of the Witwatersrand, Johannesburg. pp. 133.
Cornell, D.H., Schütte, S.S., Eglington, B.L., 1996. The Ongeluk basaltic andesite formation in Griqualand West, South Africa: submarine alteration in a 2222 Ma Proterozoic sea. Precambr. Res. 79, 101–123.
Des Marais, D.J., Strauss, H., Summons, R.E., Hayes, J.M., 1992. Carbon isotope evidence for the stepwise oxidation of the Proterozoic environment. Nature 359, 605–609.
Dorland, D.H., 2004. Provenance Ages and Timing of Sedimentation of Selected Neoarchean and Paleoproterozoic Successions on the Kaapvaal Craton. PhD thesis (unpublished). University of Johannesburg, pp. 326.
Eriksson, P.G., Altermann, W., Hartzer, F.J., 2006. The Transvaal Supergroup and its precursors. In: Johnson, M.R., Anhaeusser, C.R., Thomas, R.J. (Eds.), The Geology of South Africa. Geological Society of South Africa, Johannesburg/Council for Geoscience, Pretoria, pp. 237–260.
Eroglu, S., Schoenberg, R., Wille, M., Beukes, N., Taubald, H., 2015. Geochemical stratigraphy, sedimentology, and Mo isotope systematics of the ca. 2.58–2.50 Ga-old transvaal Supergroup carbonate platform, South Africa. Precambr. Res. 266, 27–46.
Eroglu, S., van Zuilen, M.A., Taubald, H., Drost, K., Wille, M., Swanner, E.D., Beukes, N.J., Schoenberg, R., 2017. Depth-dependent δ13C trends in platform and slope settings of the Campbellrand-Malmani carbonate platform and possible implications for Early Earth oxygenation. Precambr. Res. 302, 122–139.
Evans, D.A., Beukes, N.J., Kirschvink, J.L., 1997. Low-latitude glaciation in the Palaeoproterozoic era. Nature 386, 262–266.
Farquhar, J., Bao, H., Thiemens, M., 2000. Atmospheric influence of earth's earliest sulfur cycle. Science 289, 756–758.
Farquhar, J., Peters, M., Johnston, D.T., Strauss, H., Masterson, A., Wiechert, U., Kaufman, A.M., 2007. Isotopic evidence for Mesoachaean anoxia and changing atmospheric sulphur chemistry. Nature 449, 706–710.
Fischer, W.W., Schroeder, S., Lacassie, J.P., Beukes, N.J., Goldberg, T., Strauss, H., Horstmann, U.E., Schrag, D.P., Knoll, A.H., 2009. Isotopic constraints on the Late Archean carbon cycle from the Transvaal Supergroup along the western margin of the Kaapvaal Craton, South Africa. Precambr. Res. 169, 15–27.
Frauenstein, F., Veizer, J., Beukes, N., Van Niekerk, H.S., Coetzee, L.L., 2009. Transvaal Supergroup carbonates: implications for Paleoproterozoic $\delta^{18}O$ and $\delta^{13}C$ records. Precambr. Res. 175, 149–160.
Friedman, G.M., 1965. Terminology of recrystallization textures and fabrics in sedimentary rocks. J. Sediment. Petrol. 35, 643–655.
Ghent, E.D., O'Neil, J.R., 1985. Late precambrian marbles of unusual carbon-isotope composition, southeastern British Columbia. Can. J. Earth Sci. 22, 324–329.
Godfrey, L.V., Falkowski, P.G., 2009. The cycling and redox state of nitrogen in the Archaean ocean. Nat. Geosci. 2, 725–729.
Gregg, J.M., Sibley, D.F., 1984. Epigenetic dolomitization and the origin of xenotopic dolomite texture. J. Sediment. Res. 54, 908–931.
Gumsley, A.P., Chamberlain, K.R., Bleeker, W., Söderlund, U., De Kock, M.O., Larsson, E.R., Bekker, A., 2017. Timing and tempo of the great oxidation event. Proc. Natl. Acad. Sci. 114, 1811–1816.
Guo, Q., Strauss, H., Kaufman, A.J., Schröder, S., Gutzmer, J., Wing, B., Baker, M.A., Bekker, A., Kim, Q., Jin, S-T., Farquhar, J., 2009. Reconstructing Earth's surface oxidation across the Archean-Proterozoic transition. Geology 37, 399–402.
Hannah, J.L., Bekker, A., Stein, H.J., Markey, R.J., Holland, H.D., 2004. Primitive Os and 2316 Ma age for marine shale: implications for Paleoproterozoic glacial events and the rise of atmospheric oxygen. Earth Planet. Sci. Lett. 225, 43–52.
Hoffman, P.F., 2013. The Great Oxidation and a Siderian snowball Earth: MIF-S based correlation of Paleoproterozoic glacial epochs. Chem. Geol. 362, 143–156.
Holland, H.D., 2002. Volcanic gases, black smokers, and the Great Oxidation Event. Geochimica et Cosmochicia Acta 66, 3811–3826.
Holland, H.D., 2006. The oxygenation of the atmosphere and oceans. Philos. Trans. R. Soc. B: Biol. Sci. 361, 903–915.
Hover Granath, V.H., Papike, J.J., Labotka, T.C., 1983. The notch peak contact metamorphic aureole, Utah: petrology of the Big Horse limestone member of the Orr formation. Geol. Soc. Am. Bull. 94, 889–906.

Kamber, B.S., Webb, G.E., Gallagher, M., 2014. The rare earth element signal in Archaean microbial carbonate: information on ocean redox and biogenicity. J. Geol. Soc. 171, 745–763.
Karhu, J.A., Holland, H.D., 1996. Carbon isotopes and the rise of atmospheric oxygen. Geology 24, 867–870.
Kerr, G.B., Prave, A.R., Martin, A.P., Fallick, A.E., Brasier, A.T., Park, R.G., 2016. The Palaeoproterozoic global carbon cycle: insights from the Loch Maree Group, NW Scotland. J. Geol. Soc. 173, 170–176.
Kendall, B., Reinhard, C.T., Lyons, T.W., Kaufman, A.J., Poulton, S.W., Anbar, A.D., 2010. Pervasive oxygenation along late Archaean ocean margins. Nat. Geosci. 3, 647–652.
Klein, C., 1983. Diagenesis and metamorphism of Precambrian banded iron-formations. Dev. Precamb. Geol. 6, 417–469.
Klein, C., 2005. Some Precambrian banded iron-formations (BIFs) from around the world: their age, geologic setting, mineralogy, metamorphism, geochemistry, and origins. Am. Mineral. 90, 1473–1499.
Klein, C., Gole, M.J., 1981. Mineralogy and petrology of parts of the Marra Mamba iron formation, Hamersley Basin, Western Australia. Am. Mineral. 66, 507–525.
Kopp, R.E., Kirschvink, J.L., Hilburn, I.A., Nash, C.Z., 2005. The Paleoproterozoic snowball Earth: a climate disaster triggered by the evolution of oxygenic photosynthesis. Proc. Natl. Acad. Sci. 102, 11131–11136.
Lawrence, M.G., Kamber, B.S., 2006. The behaviour of the rare earth elements during estuarine mixing—revisited. Mar. Chem. 100, 147–161.
Lawrence, M.G., Kamber, B.S., 2007. Corrigendum to "The behaviour of the rare earth elements during estuarine mixing—revisited" [Marine Chemistry 100 (2006) 147–161]. Mar. Chem. 105, 181.
Lawrence, M.G., Greig, A., Collerson, K.D., Kamber, B.S., 2006. Rare earth element and yttrium variability in South East Queensland waterways. Aquat. Geochem. 12, 39–72.
Luo, G., Ono, S., Beukes, N.J., Wang, D.T., Xie, S., Summons, R.E., 2016. Rapid oxygenation of Earth's atmosphere 2.33 billion years ago. Science. Advances 2, e1600134.
Lyons, T.W., Reinhard, C.T., Planavsky, N.J., 2014. The rise of oxygen in Earth's early ocean and atmosphere. Nature 506, 307–314.
Martin, D.McB., Clendenin, C.W., Krapez, B., McNaughton, N.J., 1998. Tectonic and geochronological constraints on late Archaean and Palaeoproterozoic stratigraphic correlation within and between the Kaapvaal and Pilbara cratons. J. Geol. Soc. London 155, 311–322.
Martin, A.P., Condon, D.J., Prave, A.R., Lepland, A., 2013. A review of temporal constraints for the Palaeoproterozoic large, positive carbonate carbon isotope excursion (the Lomagundi-Jatuli Event). Earth Sci. Rev. 127, 242–261.
McNaughton, N.J., Wilson, A.F., 1983. 13C-rich marbles from the Proterozoic Einasleigh metamorphics, northern Queensland. J. Geol. Soc. Aust. 30, 175–178.
Moffett, J.W., 1994. A radiotracer study of cerium and manganese uptake onto suspended particles in Chesapeake Bay. Geochim. Cosmochim. Acta 58, 695–703.
Moore, J.M., Polteau, S., Armstrong, R.A., Corfu, F., Tsikos, H., 2012. The age and correlation of the Postmasburg Group, southern Africa: Constraints from detrital zircon grains. J. Afr. Earth Sc. 64, 9–19.
Martini, J.E.J., 1979. A copper-bearing bed in the Pretoria Group in the northeastern Transvaal. Geol. Soc. South Af., Spec. Pub. 6, 65–72.
Miyano, T., Beukes, N.J., 1997. Mineralogy and Petrology of the Contact Metamorphosed Amphibole Asbestos-bearing Penge Iron Formation, Eastern Transvaal, South Africa. J. Petrol. 38, 651–676.
Miyano, T., Klein, C., 1983. Conditions of riebeckite formation in the iron-formation of the Dales Gorge Member, Hamersley Group, Western Australia. Am. Mineral. 68, 517–529.
Miyashiro, A., 1972. Metamorphism and related magmatism in plate tectonics. Am. J. Sci. 272, 629–656.
Nelson, D.R., Trendall, A.F., Altermann, W., 1999. Chronological correlations between the Pilbara and Kaapvaal cratons. Precambr. Res. 97, 165–189.
Nothdurft, L.D., Webb, G.E., Kamber, B.S., 2004. Rare earth element geochemistry of Late Devonian reefal carbonates, Canning Basin, Western Australia: confirmation of a seawater REE proxy in ancient limestones. Geochim. Cosmochim. Acta 68, 263–283.
Pavlov, A.A., Kasting, J.F., 2002. Mass-independent fractionation of sulfur isotopes in archean sediments: strong evidence for an anoxic archean atmosphere. Astrobiology 2, 27–41.
Posth, N.R., Köhler, I., Swanner, E.D., Schröder, C., Wellmann, E., Binder, B., Konhauser, K.O., Neumann, U., Berthold, C., Nowak, M., Kappler, A., 2013. Simulating Precambrian banded iron formation diagenesis. Chem. Geol. 362, 66–73.
Prokoph, A., Shields, G.A., Veizer, J., 2008. Compilation and time-series analysis of a marine carbonate δ18O, δ13C, 87Sr/86Sr and δ34S database through Earth history. Earth Sci. Rev. 87, 113–133.
Rasmussen, B., Bekker, A., Fletcher, I.R., 2013. Correlation of Palaeoproterozoic glaciations based on U-Pb zircon ages for tuff beds in the Transvaal and Huronian Supergroups. Earth Planet. Sci. Lett. 382, 173–180.
Schneiderhan, E.A., Gutzmer, J., Strauss, H., Mezger, K., Beukes, N.J., 2006. The chemostratigraphy of a Paleoproterozoic MnF-BIF succession–the Voëlwater Subgroup of the Transvaal Supergroup in Griqualand West, South Africa. S. Afr. J. Geol. 109, 63–80.
Schröder, S., Warke, M.R., 2016. Termination of BIF deposition in the Paleoproterozoic: the Tongwane Formation, South Africa. S. Afr. J. Geol. 119, 329–346.
Schröder, S., Bedorf, D., Beukes, N.J., Gutzmer, J., 2011. From BIF to red beds: sedimentology and sequence stratigraphy of the Paleoproterozoic Koegas Subgroup (South Africa). Sediment. Geol. 236, 25–44.
Schröder, S., Beukes, N.J., Armstrong, R.A., 2016. Detrital zircon constraints on the tectonostratigraphy of the Paleoproterozoic Pretoria Group, South Africa. Precambr. Res. 278, 362–393.
Sharpe, M.R., Chadwick, B., 1982. Structures in Transvaal sequence rocks within and adjacent to the eastern Bushveld Complex. Trans. Geol. Soc. South Afr. 85, 29–41.
Sibley, D.F., Gregg, J.M., 1987. Classification of dolomite rock textures. J. Sediment. Petrol. 57, 957–965.
Shields, G.A., Veizer, J., 2002. Precambrian marine carbonate isotope database: Version 1.1. Geochem. Geophys. Geosyst. 3. http://dx.doi.org/10.1029/2001GC000266.
Swart, Q.D., 1999. Carbonate rocks of the Paleoproterozoic Pretoria and Postmasburg Groups, Transvaal Supergroup. M.Sc thesis (unpublished), University of Johannesburg, pp. 126.
Taylor, S.R., McLennan, S.M., 1985. The continental crust: its composition and evolution. Blackwell Scientific Publications, Oxford, pp. 312.
Tang, D., Shi, X., Wang, X., Jiang, G., 2016. Extremely low oxygen concentration in mid-Proterozoic shallow seawaters. Precambr. Res. 276, 145–157.
Tosca, N.J., Johnson, D.T., Mushegian, A., Rothman, D.H., Summons, R.E., Knoll, A.H., 2010. Clay mineralogy, organic carbon burial, and redox evolution in Proterozoic oceans. Geochim. Cosmochim. Acta 74, 1579–1592.
Tosca, N.J., Guggenheim, S., Pufahl, P.K., 2016. An authigenic origin for Precambrian greenalite: implications for iron formation and the chemistry of ancient seawater. Geol. Soc. Am. Bull. 128, 511–530.
Tostevin, R., Shields, G.A., Tarbuck, G.M., He, T., Clarkson, M.O., Wood, R.A., 2016a. Effective use of cerium anomalies as a redox proxy in carbonate-dominated marine settings. Chem. Geol. 438, 146–162.
Tostevin, R., Wood, R.A., Shields, G.A., Poulton, S.W., Guilbaud, R., Bowyer, F., Penny, A.M., He, T., Curtis, A., Hoffmann, K.H., Clarkson, M.O., 2016b. Low-oxygen waters limited habitable space for early animals. Nat. Commun. 7. http://dx.doi.org/10.1038/ncomms12818.
Tsikos, H., Moore, J.M., Harris, C., 2001. Geochemistry of the Palaeoproterozoic Mooidraai formation: Fe-rich limestone as end member of iron formation deposition, Kalahari manganese field, Transvaal Supergroup, South Africa. J. Afr. Earth Sc. 32, 19–27.
Valley, J.W., 1986. Stable isotope geochemistry of metamorphic rocks. Rev. Mineral. Geochem. 16, 445–489.
Van Kranendonk, M.J., Webb, G.E., Kamber, B.S., 2003. Geological and trace element evidence for a marine sedimentary environment of deposition and biogenicity of 3.45 Ga stromatolitic carbonates in the Pilbara Craton, and support for a reducing Archaean ocean. Geobiology 1 (2), 91–108.
Veizer, J., 1983. Trace elements and isotopes in sedimentary carbonates. Rev. Mineral. Geochem. 11, 265–299.
Veizer, J., Clayton, R.W., Hinton, R.W., 1992. Geochemistry of Precambrian carbonates: IV. Early Paleoproterozoic (2.25 ± 0.25 Ga) seawater. Geochim. Cosmochim. Acta 56, 875–885.
Voegelin, A.R., Nägler, T.F., Beukes, N.J., Lacassie, J.P., 2010. Molybdenum isotopes in late Archaean carbonate rocks: Implications for Early Earth oxygenation. Precambr. Res. 182, 70–82.
Wachter, E.A., Hayes, J.M., 1985. Exchange of oxygen isotopes in carbon dioxide-phosporic acid systems. Chem. Geol. Isot. Geosci. Sec. 52, 365–374.
Wille, M., Kramers, J.D., Nägler, T.F., Beukes, N.J., Schröder, S., Meisel, T., Lacassie, J.P., Voegelin, A.R., 2007. Evidence for a gradual rise of oxygen between 2.6 and 2.5 Ga from Mo isotopes and Re-PGE signatures in shales. Geochim. Cosmochim. Acta 71, 2417–2435.